

Boletín Geológico, 47, 5-34, 2020  
<https://doi.org/10.32685/0120-1425/>  
boletingeo.47.2020.502



This work is distributed under the Creative Commons Attribution 4.0 License.

Received: May 17, 2020

Revised: July 9, 2020

Accepted: August 20, 2020

Published online: December 28, 2020

# The Guaviare Complex: new evidence of Mesoproterozoic (ca. 1.3 Ga) crust in the Colombian Amazonian Craton

**El Complejo Guaviare: nueva evidencia de corteza continental del Mesoproterozoico (ca. 1,3 Ga) en el Cratón Amazónico colombiano**

Carolina Amaya López<sup>1</sup>, Jorge Julián Restrepo Álvarez<sup>1</sup>, Marion Weber Scharff<sup>2</sup>, Federico Alberto Cuadros Jiménez<sup>3</sup>, Nilson Francisquini Botelho<sup>3</sup>, Mauricio Ibáñez Mejía<sup>4</sup>, Mario Maya Sánchez<sup>5</sup>, Orlando Manuel Pérez Parra<sup>6</sup>, Carlos Ramírez Cárdenas<sup>7</sup>

<sup>1</sup> Universidad Nacional de Colombia, Medellín, Colombia

<sup>2</sup> Departamento de Geociencias y Medio Ambiente, Universidad Nacional de Colombia, Medellín, Colombia

<sup>3</sup> Institute of Geosciences, Universidade de Brasília, Brazil

<sup>4</sup> Department of Earth and Environmental Sciences, University of Rochester, New York, USA

<sup>5</sup> Servicio Geológico Colombiano, Bogotá, Colombia

<sup>6</sup> Université Grenoble-Alpes, France

<sup>7</sup> Faculty of Earth Sciences, Universitat de Barcelona – UB, Spain

**Corresponding author:** Carolina Amaya, caro.geologia@gmail.com

## ABSTRACT

The Guaviare Complex is a new unit defined in the Colombian Amazonian Craton, which is part of the Precambrian basement located in southeastern Colombia. It is divided into three units according to their textural and compositional characteristics, termed Termal Gneiss, Unilla Amphibolite, and La Rompida Quartzite.

Termal Gneiss rocks are petrographically classified as gneisses and quartz-feldspar granofels, with the local formation of blastomylonite-like dynamic rocks. The Unilla Amphibolite consists of only amphibolites, and La Rompida Quartzite consists of muscovite quartzites, quartz-feldspar granofels, and quartz-muscovite schists.

The protoliths of Termal Gneiss and Unilla Amphibolite were formed in the Mesoproterozoic at 1.3 Ga due to bimodal magmatism (felsic and mafic) derived from mantle material, with some crust contamination that was probably related to the formation of extensional arcs associated with trans-arc basins in the NW section of the Amazon Craton. La Rompida Quartzite rocks originated from sediments derived from granite rocks and from other, older areas of the craton. These rocks have a maximum age of 1.28 Ga.

The low-to-medium grade metamorphism that affected these units occurred from 1.28 to 0.6 Ga, most likely concurrently with the Putumayo orogeny of approximately 1.0 Ga, although it may have been an independent event.

**Keywords:** Metamorphic Complex, Amazonian Craton, Proterozoic, Orogeny, geochemistry, geochronology.

**Citation:** Amaya López, C., Restrepo Álvarez, J. J., Weber Scharff, M., Cuadros Jiménez, F. A., Botelho, N. F., Ibáñez Mejía, M., Maya Sánchez, M., Pérez Parra, O. M., & Ramírez Cárdenas, C. (2020). The Guaviare Complex: new evidence of Mesoproterozoic (ca. 1.3 Ga) crust in the Colombian Amazonian Craton. *Boletín Geológico*, 47, 5-34, <https://doi.org/10.32685/0120-1425/boletingeo.47.2020.502>

## RESUMEN

El Complejo Guaviare es una unidad nueva definida en el Cratón Amazónico colombiano, que hace parte del basamento precámbrico situado en el suroriente del territorio colombiano. Está dividido en tres unidades, según sus características texturales y composicionales, denominadas Neis de Termiales, Anfibolita de Unilla y Cuarcita de La Rompida.

Las rocas del Neis de Termiales se clasifican petrográficamente como neises y granofelsas cuarzo-feldespáticas, localmente con formación de rocas dinámicas tipo blastomilonitas. La Anfibolita de Unilla está representada únicamente por anfibolitas, y la Cuarcita de La Rompida, por cuarcitas moscovíticas, granofelsas cuarzo-feldespáticas y esquistos cuarzo-moscovíticos.

Los protolitos del Neis de Termiales y la Anfibolita de Unilla se formaron en el Mesoproterozoico, hace 1,3 Ga, por un magmatismo bimodal (félscico y máfico) derivado de material mantélico con alguna contaminación cortical, probablemente relacionado con la formación de arcos extensionales asociados a cuencas trasarco en la parte NW del Cratón Amazónico. Las rocas de la Cuarcita de La Rompida se originaron a partir de sedimentos derivados de las rocas graníticas y de otras áreas más antiguas del cráton. Estas rocas tienen una edad máxima de 1,28 Ga.

El metamorfismo de bajo a medio grado que afectó estas unidades tuvo lugar entre 1,28 Ga y 0,6 Ga, y es probable que ocurriera al mismo tiempo que la Orógeno Putumayo, alrededor de 1,0 Ga, aunque no se puede descartar que sea un evento independiente.

**Palabras clave:** Complejo Metamórfico, Cratón Amazónico, Proterozoico, Orogenia, Geoquímica, Geocronología.

## 1. INTRODUCTION

In the department of Guaviare, Colombia, in an area between the Mitú Complex (López et al., 2007; Rodríguez et al., 2011a, 2011b) and the Garzón Complex (Rodríguez et al., 2003), metamorphic rocks have been identified, consisting of quartz-feldspar gneisses, amphibolites, quartzites, and granofels. By their compositional and textural characteristics, they are grouped into three lithological units, termed here Termales Gneiss, Unilla Amphibolite, and La Rompida Quartzite.

These rocks were first studied by Buchely et al. (2015) in Plate 371, Puerto Cachicamo, located west of Plate 372. They performed a macroscopic and microscopic description of rocks with gneissic structure. Despite their distance from the Garzón Massif, these rocks were termed the Garzón Complex.

In this study, petrographic characterization, geochemical analysis of major and trace elements, and uranium–lead (U–Pb) zircon geochronology was performed for each of the lithological units that make up the Guaviare Complex. The findings enable to understand the formation environment and petrogenesis of the complex with an eye towards defining a new metamorphic unit.

## 2. METHOD

### 2.1 Field geology and petrography

The field study was conducted in the Amazon region between the municipalities of San José del Guaviare and Calamar, in the department of Guaviare, during the geological mapping project of Plate 372 – El Retorno, conducted by Serviminas S. A. S. from 2017 to 2019 for the Servicio Geológico Colombiano – SGC. The geological survey was performed on topographic maps of the Instituto Geográfico Agustín Codazzi (Geographic Institute Agustín Codazzi) at a 1:25,000 scale following the parameters for field data collection proposed by Caicedo (2003) and updated by Serviminas S. A. S. (Maya et al., 2019). In total, at 40 field stations, 47 rock samples of gneiss, granofels, amphibolite, quartzite, schist, and blastomylonite were collected in the Guaviare Complex. 42 thin sections were prepared and analyzed by transmission light microscopy at 300 points for each sample. The minerals, textures, paragenesis, protoliths, metamorphic facies, and type and degree of metamorphism were described based on Heinrich (1965), Winkler (1976), Bowie and Simpson (1977), Winter (2001), and Schmid et al. (2007).

### 2.2 Geochemistry

Geochemical analyses of major and trace elements, including rare-earth elements, were performed by X-ray fluorescence (XRF) and inductively coupled plasma mass spectrometry

(ICP-MS) at ALS Global Ltd., according to the internal code specifications of the laboratory (ME-XRF26 and ME-MS81). The samples were crushed and pulverized, and the fraction smaller than 200 mesh was collected. The analyses were performed following laboratory standards, including sample fusion with LiBO<sub>2</sub> and acid digestion for ICP-MS.

### 2.3 Total rock analysis

Isotopic analyses of Sm, Nd, and Sr were performed at the Geochronology and Isotopic Geochemistry Laboratory of the Universidad de Brasilia. The analytical procedures applied in this study to determine the <sup>147</sup>Sm/<sup>144</sup>Nd, and <sup>143</sup>Nd/<sup>144</sup>Nd isotopic ratios were described by Gioia and Pimentel (2000). <sup>149</sup>Sm and <sup>150</sup>Nd spike solutions were added to the crushed and pulverized rock samples. Sm and Nd were separated using cation exchange columns. Then, two drops of 0.025N H<sub>3</sub>PO<sub>4</sub> were added to the resulting fractions for subsequent evaporation. The residue was dissolved in 1 µl of 5% HNO<sub>3</sub> distillate and mounted on a double-rhenium filament inside a Finnigan MAT 262 mass spectrometer with seven collectors in static mode. The uncertainties of the <sup>147</sup>Sm/<sup>144</sup>Nd and <sup>143</sup>Nd/<sup>144</sup>Nd isotopic ratios were lower than 0.2% and 0.0029% (2σ), respectively, based on the analysis of the international standard BHVO-2. The <sup>143</sup>Nd/<sup>144</sup>Nd ratio was normalized using the ratio <sup>146</sup>Nd/<sup>144</sup>Nd = 0.7219 and the decay constant  $6.54 \times 10^{-12} \text{ a}^{-1}$  (Lugmair and Marti, 1978).

The procedures followed for the Sr isotopic analyses were as described by Gioia et al. (1999). The samples were pulverized and subjected to acid attack under different solutions of HF, HNO<sub>3</sub>, and HCl, with subsequent separation in cation exchange columns. Then, fractions containing Sr were deposited together with 1 µl of H<sub>3</sub>PO<sub>4</sub> in a tantalum filament in the mass spectrometer described above. Based on the analysis of the international standard NBS-987, the uncertainties assessed for the <sup>87</sup>Sr/<sup>86</sup>Sr ratio were lower than 0.0078% (2σ). The <sup>87</sup>Rb/<sup>86</sup>Sr ratio was calculated based on the concentrations of Rb and Sr determined by ICP-MS in the samples (annex 1), according to the procedure indicated by Faure and Mensing (2005).

### 2.4 LA-ICP-MS U-Pb zircon geochronology

The samples were initially prepared at the Universidad EA-FIT, where zircon crystals were separated and then subjected to standard ore crushing, sieving, and concentration methods. Later, at the University of Rochester, several crystals of each sample were mounted in epoxy resin and polished to expose an internal face on which textural and isotopic analyses would be

performed. Cathodoluminescence images, acquired to reveal the internal structure of the zircons and to guide the geochronological analyses, were recorded under a Jeol 7100FT scanning electron microscope with a field emission source and a Deben panchromatic cathodoluminescence detector at the Mackay Microbeam Laboratory, University of Nevada, Reno.

The U-Pb isotopic analyses were conducted at the University of Rochester using an Agilent 7900 ICP-MS coupled to a Photon Machine Analyte G2 laser ablation system, which features a HelEx2 quick-purge tunable two-volume LA-ICP-MS cell system and generates pulses lasting approximately 8 ns using an excited ArF dimer. During the analyses, the laser was operated at a 7-Hz repetition rate and at a spot diameter of 30 µm, generating a constant energy density of approximately 7 J/cm<sup>2</sup> on the surface of the analyzed crystals. The ablations were conducted in an ultra-high-purity helium atmosphere, which was the gas used to transport the ablation aerosol to the ICP-MS. Each analysis consisted of 15 seconds of measurement of the “analytical blank” with the laser off, immediately followed by a 20-second measurement of the isotopic composition of the crystals with the laser on. <sup>202</sup>Hg, <sup>204</sup>(Pb+Hg), <sup>206</sup>Pb, <sup>207</sup>Pb, <sup>208</sup>Pb, <sup>232</sup>Th, and <sup>238</sup>U isotopes were measured in the mass spectrometer, and instrumental bias was corrected using the standard-sample bracketing method and using fragments of a zircon from Sri Lanka (SL2) with a known age of 563.6 ± 3.2 Ma, assessed following the reference manual Isotope Dilution - Thermal Ionization Mass Spectrometry, (Gehrels et al., 2008).

U-Pb data were processed using the procedures and algorithms described by Pullen et al. (2018) to make the necessary linearity corrections of the detection system. In addition to the primary reference material and to zircons from the Guaviare Complex, during our analytical session, several zircon fragments from Plešovice and FC-1 (Duluth gabbro, Minnesota, USA) were also analyzed to evaluate the precision, accuracy, and reproducibility of the method. These secondary materials yielded weighted mean ages of <sup>206</sup>Pb/<sup>238</sup>U = 335.0 ± 1.2/3.9 (2σ, n = 21, mean squared weighted deviation (MSWD) = 0.8) for Plešovice and <sup>207</sup>Pb/<sup>206</sup>Pb = 1098 ± 8/11 (2σ, n = 23, MSWD = 0.3) for FC-1, where the first level of uncertainty reported represents only internal analytical uncertainties, and the second level of uncertainty includes the propagation of systematic and standardization-related sources of uncertainty. After including systematic uncertainties, the values from our analytical session were indistinguishable from the reference ages of 337.13 ± 0.37 Ma for Plešovice (Sláma et al., 2008) and of 1099.96 ±

0.58 Ma for FC-1 (Ibáñez Mejía and Tissot, 2019), assessed following the Chemical Abrasion - Isotope Dilution - Thermal Ionization Mass Spectrometry reference, which confirms that the geochronological results reported in this study are accurate and that the analytical uncertainties have been correctly assigned.

### 3. GEOLOGICAL FRAMEWORK

The Guaviare Complex is the lithodemic unit that forms the crystalline basement of southeastern Colombia and groups the regional metamorphic rocks of the Mesoproterozoic described in Plate 372 – El Retorno (Maya et al., 2018) and Plate 371 – Puerto Cachicamo (Buchely et al., 2015). In southeastern Colombia, two main units of Precambrian metamorphic rocks have been regionally defined, the Mitú Migmatite Complex (Galvis et al., 1979; Rodríguez et al., 2011a) or Mitú Complex (López et al., 2007) in the NW section of the Amazonian Craton (or Guiana Shield) and the Garzón Complex in the Andes mountain range (Rodríguez et al., 2003; Cordani et al., 2005; Ibáñez Mejía et al., 2011, 2015).

In the Mitú Complex, the initial Rb-Sr and K-Ar radiometric dates were reanalyzed by Cordani et al. (2016) and complemented with new, more robust zircon U-Pb dating, which identified two belts of different ages: the Atabapo Belt to the north, with ages from 1800 to 1740 Ma, and the Vaupés Belt to the south, with granitoids of 1580 to 1520 Ma. The metamorphic rocks of Araracuara have ages similar to those of the Vaupés Belt. In this area, K-Ar dating has recorded an intra-plate heating event dated from 1200 to 1300 Ma, termed the *Nickerian event*. Based on the nomenclature developed by Cordani et al. (1979) and by Tassinari and Macambira (1999), by age and position, the rocks of the Mitú Complex are part of the Rio Negro-Juruena province. With these new dating results, the concept of a Mitú Complex or Mitú Migmatitic Complex becomes obsolete and should no longer be used (see also Ibáñez Mejía and Cordani, 2020).

In studies of the Garzón Massif, the Macarena mountain range, and the basement of the Putumayo basin, Ibáñez Mejía et al. (2011, 2015, 2018) have reported ages that show that this area was formed between 1300 and 990 Ma. Thus, a juvenile intraoceanic magmatic arc developed from 1300 to 1200 Ma, followed by two metamorphic events: a migmatization event in amphibolite facies, which occurred between approximately

1050 and 1010 Ma, and another event in granulite facies, which occurred approximately 990 Ma. Although this area is chronologically similar to the Amazonian province of Sunsás, its origin and location are very different. For this reason, the aforementioned authors consider that this area is a new province of the Amazonian Craton, which they term *Putumayo Orogen*.

The Guaviare Complex is located in an intermediate area between the outcrops of the Atabapo and Vaupés Belts to the east and the Garzón Complex to the west (Figure 1 a, b). Therefore, it may be correlated with some of these units. Buchely et al. (2015) considered that the gneissic metamorphic rocks exposed in Plate 371 - Puerto Cachicamo are part of the Garzón Complex, but they did not perform radiometric dating.

### 4. RESULTS

#### 4.1 Lithology

In the Guaviare Complex, the most common lithologies are quartz-feldspar gneisses and quartzites, with local amphibolites and granofels. These rocks compose three lithological units that crop out in an elongated belt of approximately 32 km in length in a north-south direction and that stand out from the Phanerozoic sedimentary cover (Figure 2).

The Termales Gneiss encompasses gneisses and quartz-feldspar granofels. The gneisses have homogeneous foliation, ranging from slight to well marked (Figure 3 a, b), without defining a tectonic layer and with medium to very coarse grain size. They consist of feldspar, quartz, biotite, and, in small amounts, amphibole. The granofels are similar in composition to the gneisses and are found in the form of lenses with sharp contacts and a metric character. They are characterized by the absence of schistosity. Their grain size is medium, and they consist of feldspars and quartz. These rocks are associated with veins and medium-grain quartz lenses, fractured and stained by iron oxides.

The amphibolites are dark gray with medium grain size (Figure 3 c, d). They are homogeneous and slightly foliated, consisting of dark areas of amphibole and light areas of plagioclase. The quartzites are recognized for their fine to medium grain size. When somewhat weathered, they are very similar to sandstone, with a color ranging from gray to white. Some are granoblastic, and others exhibit a slight lepidoblastic schistosity. They are composed of quartz, feldspars, and muscovite, with certain levels of iron oxides. These rocks are traversed by quartz veins (Figure 3 e, f) and by a syenogranite dike.

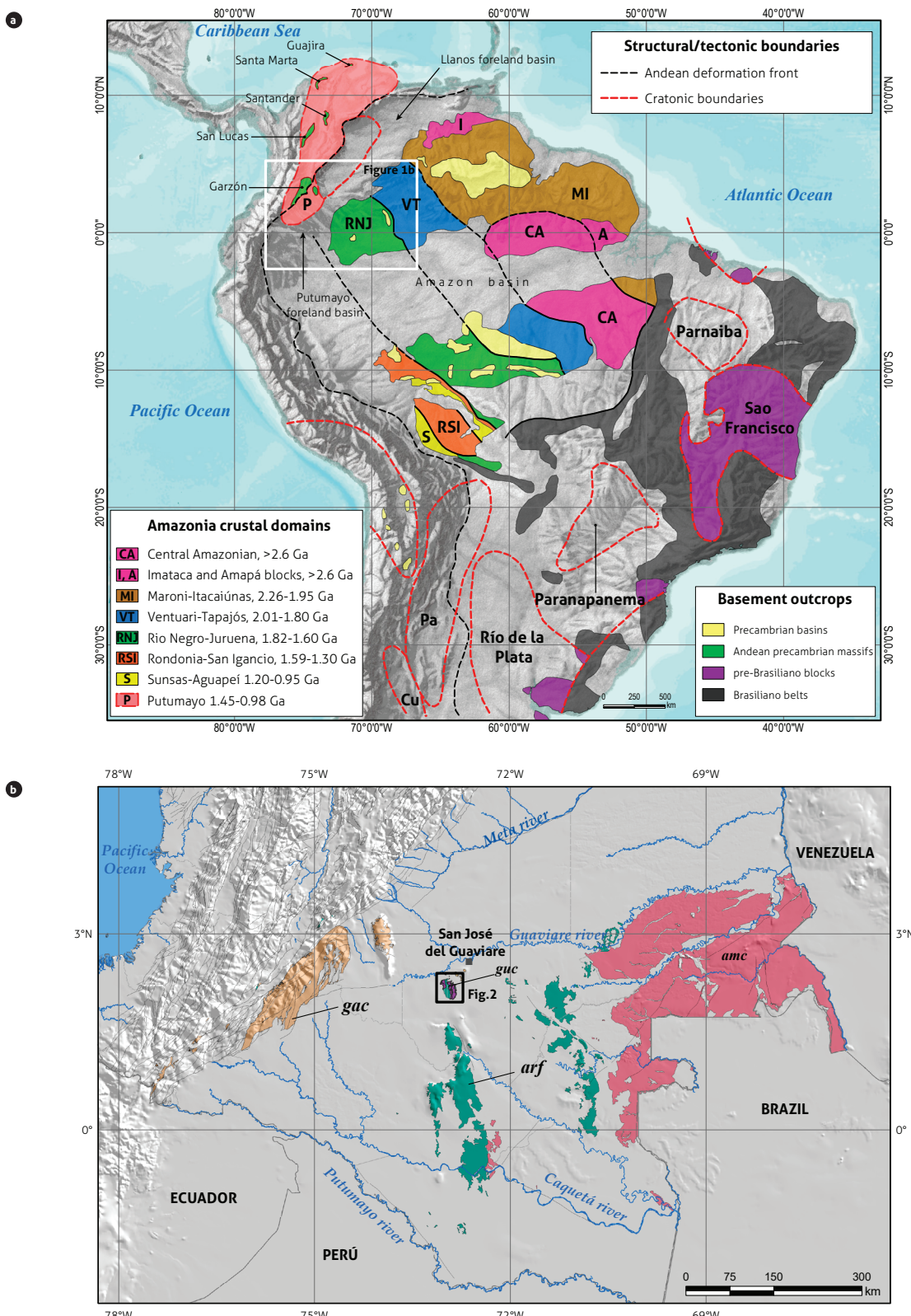


**Figure 1.** a) Location map of the Guaviare Complex in northwestern South America; b) Location map of the Guaviare Complex and metamorphic rocks located in southeastern Colombia  
guc: Guaviare Complex; gac: Garzón Complex; amc: exposed Amazonian Craton (Atabapo and Vaupés belts); arf: Araracuara Formation. Source: Modified from Ibáñez Mejía and Cordani (2020)

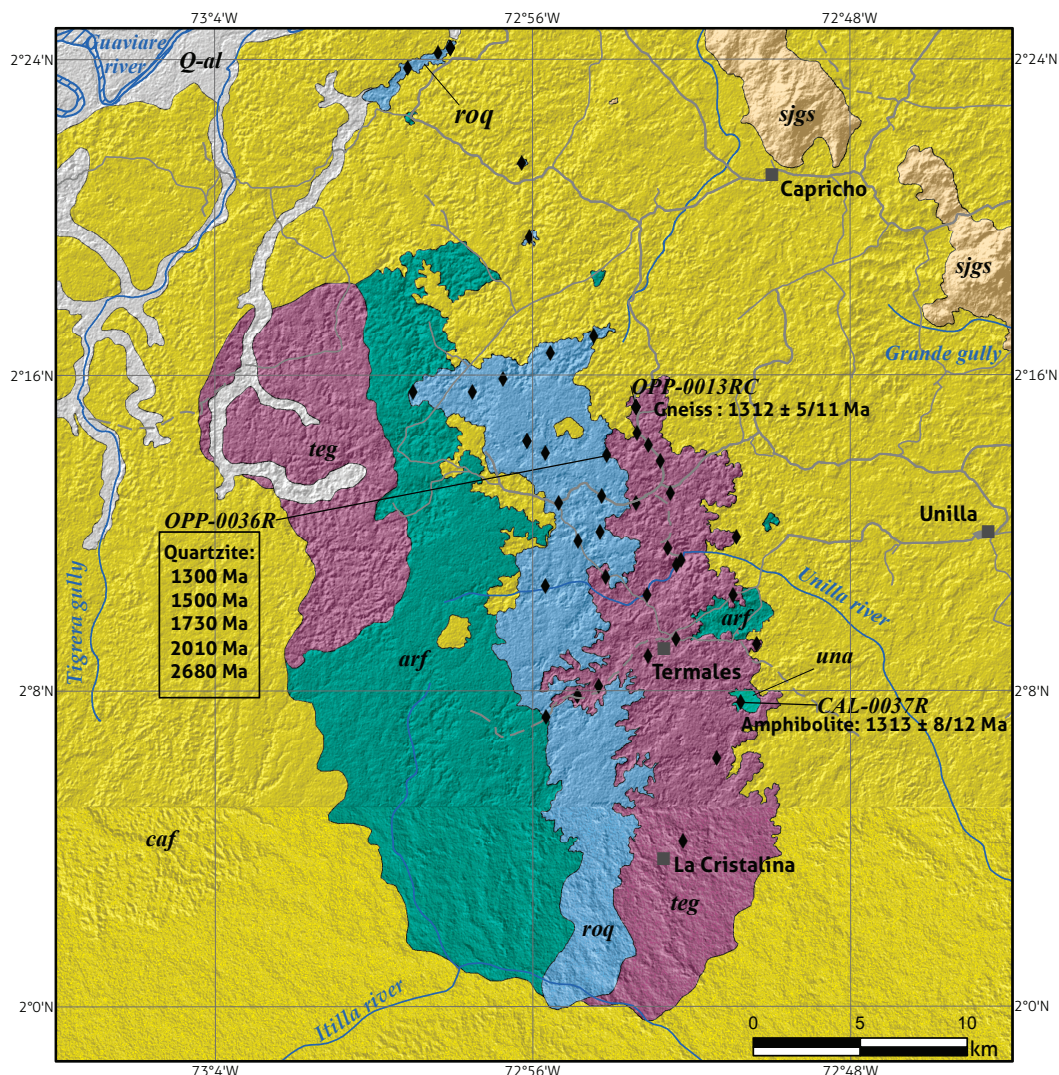


**Figure 2.** Distribution of lithological units of the Guaviare Complex  
teg: Termales Gneiss; una: Unilla Amphibolite; roq: La Rompida Quartzite; sjgs: San José del Guaviare Syenite; arf: Araracuara Formation; caf: Caja Formation; Q-al: alluvial deposits; ♦ black diamond: rock sample. Source: Modified from Maya et al. (2018)

In the Guaviare Complex, foliation is more evident in the Termales Gneiss and in the Unilla Amphibolite than in La Rompida Quartzite. In gneisses and in amphibolite, foliation ranges from N10° to 46°E, with dips ranging from 45° to 80° to the SE. The granofels contain a slight foliation of a N–S tendency with a dip to the W, in contrast to the main trend of the gneisses. In the quartzites, the N5°-to-50°E foliation with dips to the SE matches the main arrangement of the gneisses, but the dips tend to be less angled, with values ranging from 5° to 48°. A second trend, N20°-30°W, has dips to the SW and NE and could suggest a slight folding in the quartzites.

Contact between the different lithologies of the Guaviare Complex could not be established in the field due to the scarcity of outcrops. Sharp contact could only be observed between the gneisses and the granofels of Termales Gneiss. The contact between the quartzites and the gneisses could be considered discordant because the latter was a source of the sediments of the quartzite protoliths. The Araracuara Formation is located between the two metamorphic belts of the Guaviare Complex. No contact between the two units was observed in the field, but the Paleozoic sedimentary rocks likely overlay the Mesoproterozoic basement rocks (nonconformity).

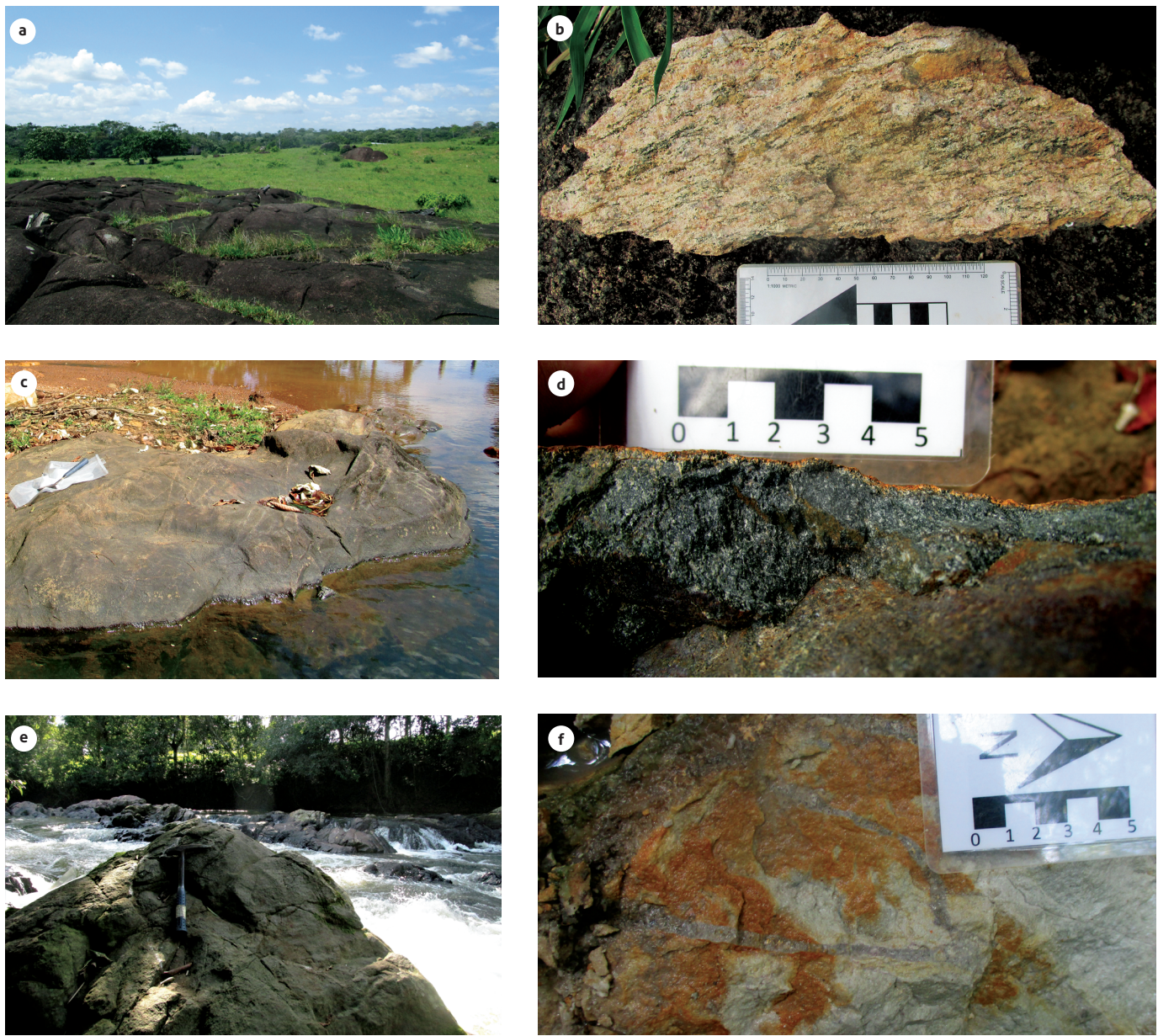


**Figure 3.** Texture and lithology of the rocks of the Guaviare Complex in macrosamples  
a and b) Quartz-feldspar gneiss. c and d) Medium-grain amphibolite. e and f) Quartzite; note the quartz veins

## 4.2 Petrography

### 4.2.1 Termales Gneiss

The Termales Gneiss comprises biotite-quartz-feldspar gneiss with  $\pm$  hornblende/hastingsite  $\pm$  epidote  $\pm$  muscovite  $\pm$  chlorite, and feldspar and quartz granofels. The mineralogical composition of the progradation consists of microcline, plagioclase, quartz, biotite, hornblende, or hastingsite and, as minor constituents, epidote, zoisite, and clinozoisite (Annex 2). The accessory

minerals are titanite, calcite, zircon, apatite, and ilmenite. The muscovite found in gneisses is considered retrograde. Common alterations include mild biotite chloritization and feldspar sericitization.

The gneisses show spaced, discontinuous, parallel and sub-parallel foliation, defined by micaceous minerals (Figure 4a) and, to a lesser extent, by amphiboles. This foliation is separated by bands of quartz-feldspar composition with a polygonal

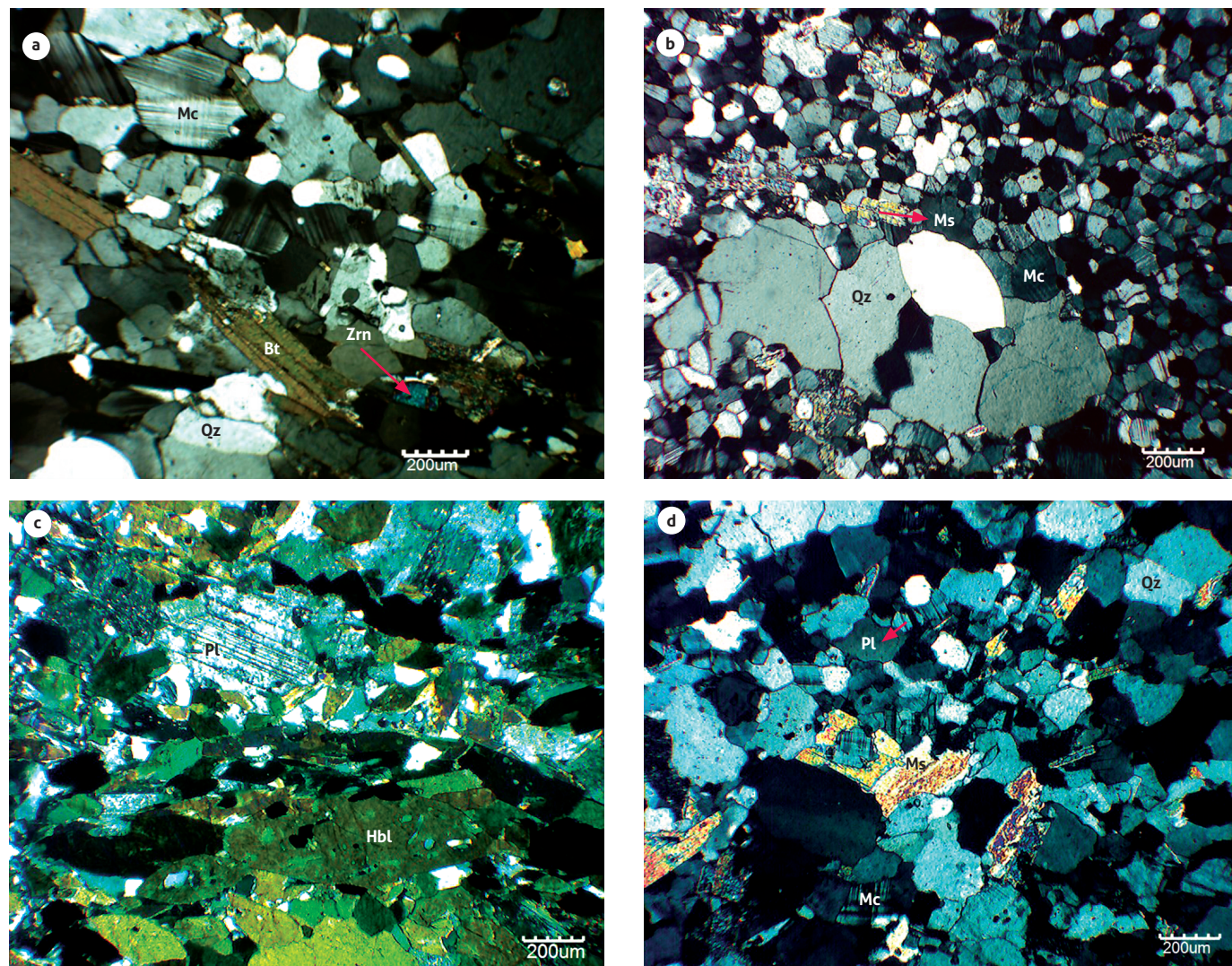


**Figure 4.** Mineralogy and texture of the rocks of the Guaviare Complex in thin sections

a) Orientation of the biotite (Bt) in the Termales Gneiss. b) Quartz (Qz) augen recrystallized in blastomylonite. c) Foliation defined by the orientation of the hornblende (Hbl) in the Unilla Amphibolite. d) Quartz (Qz), microcline (Mc) and plagioclase (Pl) forming a granoblastic texture in La Rompida Quartzite. Other abbreviations: Zrn: zircon; Ms: muscovite.

granoblastic texture. Some gneisses are characterized by the presence of quartz, plagioclase, and microcline megacrystals, which were defined as porphyroclasts derived (relict) from the original rock. In the granofels, the quartz and the plagioclase form granoblastic mosaics and exhibit deformation twins. Locally, the Termales Gneiss was affected by dynamic metamorphism, which formed blastomylonites (Figure 4b) characterized by quartz + plagioclase + microcline + garnet augen, bent twins in plagioclase, sutured edges in quartz, and embayment and skeletal texture in muscovite.

The microcline and plagioclase crystals range from subidioblastic to xenoblastic, tabular, with poikiloblastic texture (epidote, biotite, quartz and zircon inclusions), and the elongation of the crystals matches the preferential orientation of the rock. The microcline exhibits lattice twinning, whereas the plagioclase presents albite twinning, with a composition ranging from albite to oligoclase as determined using the Michel-Levy method. In the porphyroclastic gneisses, the quartz, plagioclase, and microcline crystals are characterized by their grain size variation, some reaching 7 mm in diameter. They are interna-

lly recrystallized and surrounded by quartz crystals, feldspars, and smaller micas and have a polygonal granoblastic texture.

The quartz is xenoblastic, with undulatory extinction and grain size variation. The biotite occurs as laminar, subidioblastic crystals, which define its foliation, and it shows strong pleochroism with X ( $\alpha$ ): very pale yellowish brown; and Y ( $\beta$ ) = Z ( $\gamma$ ): dark brownish green. The muscovite ranges from laminar subidioblastic to xenoblastic; some of it follows the preferential orientation of the rock, whereas other parts are disordered and replace biotite and feldspar crystals, suggesting retrograde metamorphic conditions.

The hornblende is the most common amphibole in most samples and defines nematoblastic foliation. The crystals are subidioblastic, columnar, with strong pleochroism with X ( $\alpha$ ): greenish yellow; Z ( $\gamma$ ): bluish green; and Y ( $\beta$ ): brownish greenish yellow. The hornblende is associated with biotite, zoisite, and titanite. Only in one sample (CMR-0041R) was the amphibole of the hastingsite type and occurred in subidioblastic to idioblastic, columnar crystals, with strong pleochroism with X ( $\alpha$ ): light yellow; ( $\beta$ ): bluish green; and Z ( $\gamma$ ): emerald green and quartz and zircon inclusions. This sample was characterized by high plagioclase content, low quartz content, and almost no potassium feldspar or biotite (Annex 2).

Accessory minerals such as titanite are usually found in granular agglomerations around ilmenite, whereas zircon occurs in very well-formed, prismatic, idioblastic crystals.

The mineral paragenesis of the Termales Gneiss is quartz + microcline + plagioclase (oligoclase or albite) + biotite  $\pm$  amphibole (hornblende or hastingsite). The protolith of these rocks is igneous plutonic quartz-feldspar, which underwent medium to high regional metamorphism into amphibolite facies with a locally overlayed dynamic metamorphism. Muscovite replacement in feldspars and in biotite indicates retrograde metamorphic conditions.

#### 4.2.2 Unilla Amphibolite

The Unilla Amphibolite shows spaced, coarse, and anastomosed schistosity, defined by a hornblende orientation (Figure 4c). Mineralogically, it consists of plagioclase, hornblende, quartz, biotite, retrograde chlorite, and (retrograde?) epidote and zoisite (Annex 2). The accessory minerals are apatite, titanite, and opaque (ilmenite/magnetite). Moderate plagioclase saussuritization, which makes it difficult to identify the composition, biotite chloritization, and possibly epidote and zoisite formations stand out among the alteration processes.

The plagioclase is found in tabular, subidioblastic to xenoblastic crystals with albite twinning. The quartz is xenoblastic with undulatory extinction and apatite microinclusions. The hornblende crystals range from subidioblastic to idioblastic and are columnar and orientated, with simple twinning, quartz inclusions, and strong pleochroism: X ( $\alpha$ ): yellowish green; ( $\beta$ ): olive green; and Z ( $\gamma$ ): bluish green. The biotite is arranged in subidioblastic, laminar crystals with moderate pleochroism: X ( $\alpha$ ): greenish yellow; ( $\beta$ ) = Z ( $\gamma$ ): reddish brown. Sometimes the biotite is replaced by xenoblastic to subidioblastic, laminar, oriented, and eventually flexed chlorite. The epidote is related to hornblende and chlorite domains. Among the accessory minerals, titanite is associated with oxides (ilmenite) and with amphibole and chlorite domains; opaque minerals follow foliation.

The mineral paragenesis of the Unilla Amphibolite is hornblende + plagioclase + quartz + biotite. The rock protolith is mafic igneous and was affected by medium to high regional metamorphism (?) in amphibolite facies. Chlorite replacement in biotite indicates retrograde metamorphic conditions. Although the nature of the epidote and zoisite could not be clearly established, if it were retrograde, the rock could have reached the top of the amphibolite facies.

#### 4.2.3 La Rompida Quartzite

These rocks are petrographically classified as muscovite quartzites, quartz, feldspar, and muscovite granofels and quartz and muscovite schist. They have polygonal granoblastic texture (Figure 4d) with sutured edges and embayment between crystals. Sometimes, they show textural variation with parallel to subparallel, discontinuous, anastomosed schistosity defined by muscovite. Mineralogically, they consist of quartz, plagioclase, microcline, muscovite, and chlorite. The accessory minerals include tourmaline, zircon, titanite, apatite, epidote, and opaque minerals. The feldspars are usually altered to sericite, with an intensity ranging from mild to high.

The quartz is arranged as xenoblastic crystals with undulatory extinction, in polygonal granoblastic mosaics, which vary to a granoblastic texture with sutured edges and concave-convex contacts. The feldspars are tabular, ranging from subidioblastic to xenoblastic, with lattice twinning in the microcline and albite twinning in the plagioclase of albite composition, as determined using the Michel-Levy method. The muscovite is prograde, ranging from subidioblastic to xenoblastic; laminar; sometimes disordered, with irregular edges; and usually pre-

sent in decussate agglomerations. In schist quartzites, the muscovite suggests a folded foliation, which would indicate that the rock is polyphasic. Chlorite is found as subhedral crystals present in alteration zones, interspersed with muscovite, possibly of retrograde origin.

The mineral paragenesis of La Rompida Quartzite is quartz + muscovite  $\pm$  plagioclase (albite)  $\pm$  microcline. The compositional and textural characteristics of the rocks suggest sandy sedimentary protoliths of quartzarenites and arkoses with some clay material, which underwent low to medium regional metamorphism in green schist or low-amphibolite facies. Stable muscovite in the presence of quartz indicates that the rock did not reach the top of the amphibolite facies.

#### 4.3 Geochemistry

In the Guaviare Complex, twelve metamorphic rock samples with igneous protoliths were analyzed to determine the major, minor, and trace elements (Annex 1). Eleven of them belong to the Termal Gneiss and one to the Unilla Amphibolite.

The metamorphic rocks of the Termal Gneiss were formed from felsic protoliths, which are mostly classified as granitoids, in addition to a syenite, according to the TAS classification (Cox et al., 1979). The protolith of the Unilla Amphibolite is classified as part of the gabbro field (Figure 5).

The rocks of the Termal Gneiss generally have a high  $\text{SiO}_2$  content (from 64.59% to 77.62%) and are impoverished in  $\text{Fe}_2\text{O}_3$  (from 2.65% to 3.75%),  $\text{MgO}$  (from 0.06% to 0.54%),  $\text{P}_2\text{O}_5$  (from 0.03% to 0.06%), and  $\text{TiO}_2$  (from 0.33% to 0.45%). Most of them were chemically classified as monzogranites. These samples have a relatively homogeneous behavior. Three of the samples (CMR-0041R, OPP-0013RA, OPP-0047R) differ from the main group in compounds such as  $\text{SiO}_2$ ,  $\text{Al}_2\text{O}_3$ ,  $\text{CaO}$ ,  $\text{K}_2\text{O}$ , and  $\text{Na}_2\text{O}$ . Among them, the samples CMR-0041R and OPP-0047R are chemically classified as tonalites and quartzdiorite, respectively, and petrographically they have a high plagioclase content and the highest modal amphibole content, while the sample OPP-0013RA is trondhjemite granofels with 70% oligoclase.

The samples of the main group have a  $\text{SiO}_2$  content of approximately 73% and a  $\text{Na}_2\text{O}$  content of approximately 3.3%. However, the  $\text{K}_2\text{O}$  content of the samples is more variable, ranging from 3.76% to 6.19%. The tonalite-quartzdiorite samples are characterized by a low  $\text{K}_2\text{O}$  content and the highest  $\text{Na}_2\text{O}$  content. Samples CMR-0041R and OPP-0047R have the lowest and highest  $\text{SiO}_2$  values, respectively (64.6% and 77.6%), along

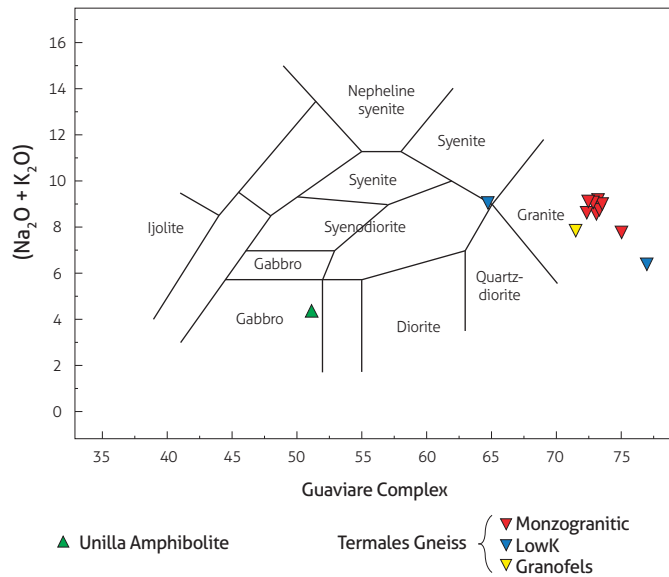
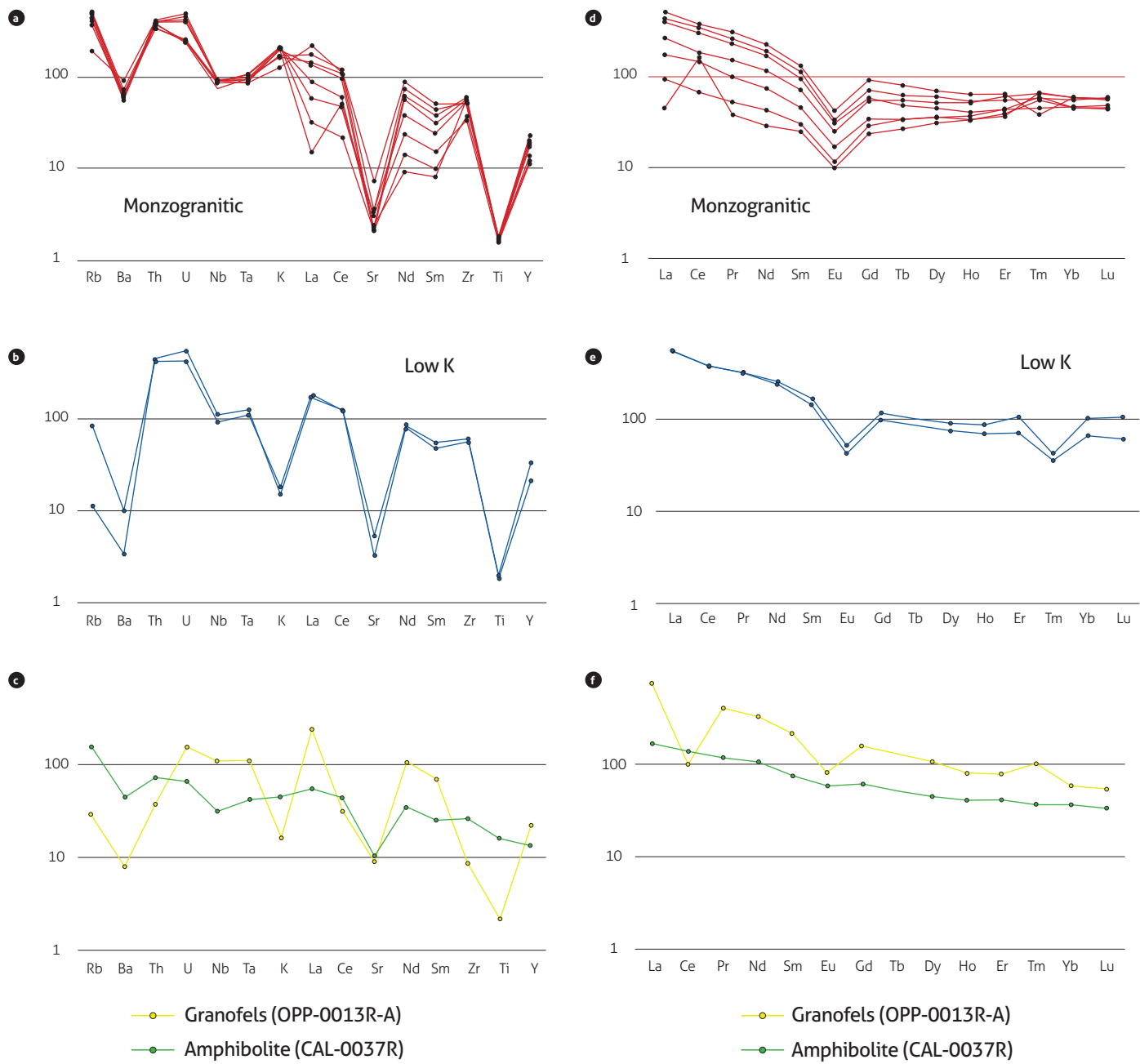


Figure 5. TAS Diagram (Cox et al., 1979) of the protoliths of rocks from the Guaviare Complex

with  $\text{Na}_2\text{O}$  values of 5.86% to 8.58% and  $\text{K}_2\text{O}$  values of 0.44% to 0.53%. Sample OPP-0013RA has  $\text{SiO}_2 = 71\%$ ,  $\text{Na}_2\text{O} = 7.26\%$ , and  $\text{K}_2\text{O} = 0.47\%$ . The sample of the Unilla Amphibolite (CAL-0037R) has low levels of  $\text{SiO}_2$  (51.0%) and alkali ( $\text{K}_2\text{O} = 1.29\%$ ;  $\text{Na}_2\text{O} = 3.05\%$ ) and high levels of  $\text{CaO}$  (7.14%),  $\text{Fe}_2\text{O}_3$  (16.01%),  $\text{MgO}$  (3.36%), and  $\text{TiO}_2$  (3.37%).

In the primitive mantle-normalized multielement plots of McDonough et al. (1992) (Figure 6), the pattern of the main group of the Termal Gneiss is homogeneous, and the samples cluster around the same values, except for rare earth elements (REEs) (La, Ce, Nd and Sm), whose values show variable enrichments in light (LREEs) and intermediate rare earth elements (IREEs) (Figure 6a). This diagram shows negative Ba, Sr, and Ti anomalies. The pattern of the samples CMR-0041R and OPP-0047R is homogeneous, with values scattered around some elements. The normalized Rb values are low, in comparison with those of the main group. The Ba anomaly is much more marked, with negative K, Sr, and Ti anomalies (Figure 6b). The sample OPP-0013RA differs from those, having a lower slope and very low U, Th, and Zr values (Figure 6c). The sample from the Unilla Amphibolite has a relatively flat pattern, it slightly enriched in the most incompatible elements, has slight negative Ba and Nb anomalies, and has a markedly negative Sr anomaly (Figure 6c).

The chondrite-normalized REE patterns of McDonough and Sun (1995) in the Termal Gneiss show variable enrich-



**Figure 6.** Multielement plots of the Termales Gneiss and Unilla Amphibolite  
a, b, and c) Primitive mantle-normalized (McDonough et al., 1992). d, e, and f) Chondrite-normalized (McDonough and Sun, 1995)

ments of LREE (Figure 6). The negative Eu anomaly stands out. This anomaly likely corresponds to rocks from which plagioclase was extracted.

In the main group (Figure 6d), the slope is negative and ranges from gentle to very gentle with  $(\text{La/Yb})_{\text{N}} = 1.0$  to 16.4, with a marked variation in LREEs and little variation

in heavy rare earth element (HREEs) ( $\text{Yb} = 5.84$  to 9.61). Both characteristics define a fan pattern radiating from the HREEs, which can be interpreted as the result of different degrees of partial fusion from the same source, wherein the samples more enriched in LREEs represent a lower degree of partial fusion than the less enriched samples, although this pa-

ttern could also have occurred due to different levels of assimilation of more differentiated materials. The low- $K_2O$  samples (Figure 6e) are similar to the most enriched LREE fraction of the main group and have a similar pattern; the slope is negative and smooth with  $(La/Yb)_N = 5.1$  to 12.8. Some samples show a negative Ce anomaly (OPP-0013RA and OPP-0013RB), whereas one shows a positive Ce anomaly (OPP-0037R), which may be related to zircon fractionation.

The amphibolite sample is enriched in LREEs, and the REE pattern has a gentle slope  $(La/Yb)_N = 4.5$ . The negative Sr (Figure 6c) and very slight Eu anomalies (Figure 6f) also suggest plagioclase removal during the fractional crystallization process of the basaltic protolith. However, these classifications should be viewed with skepticism because they are based on a single sample.

In the classification proposed to define ferrous granitoids (*sensu* Frost and Frost, 2011), also known as type A granites (see Bonin, 2007), the main rock group of the Termalas Gneiss is classified as ferrous, calc-alkaline metaluminous rocks (Figure 7). According to Frost and Frost (2011), this type of rock is formed from the differentiation of basaltic magmas that interact with crustal material (Figure 7). One of the samples of the main group is slightly peraluminous (OPP-0013RB), which may be due to increased crustal input. Importantly, this field sample was in contact with granofels. The samples CMR-0041R, OPP-013RA, and OPP-0047R range from ferrous alkaline and calc-alkaline to calcic, which reflects the variability of these three rocks. Nevertheless, the three rocks are peraluminous, and they may belong to the same magmatic suite that originated the main group and may have resulted from a greater assimilation of continental crust or from incomplete mixing with granitic magmas (Frost and Frost, 2011). However, the available data do not allow us to confirm this interpretation.

Immobile elements were used for the tectonic discrimination of the Unilla Amphibolite protolith according to the diagram of Meschede (1986) (Figure 8), in which the sample belongs to the field of within-plate tholeiites or volcanic arc basalts. Due to the primitive mantle- and chondrite-normalized flat pattern of trace elements and REEs, it is considered that the formation environment corresponded to a within-plate or volcanic-arc environment.

The geochemistry of most rocks of the Termalas Gneiss is characterized by monzogranitic compositions and presents little geochemical variation. The ASI and  $Na_2O+K_2O-CaO$  values differ from those assessed in ferrous magmas in partial fusion

experiments of shallow crust (e.g., Patiño-Douce, 1997; Skjelbreia and Johnston, 1993), suggesting a mantle contribution in the formation of the protoliths of these rocks. Only the sample of granofels with a trondhjemite composition resembles this type of melted material.

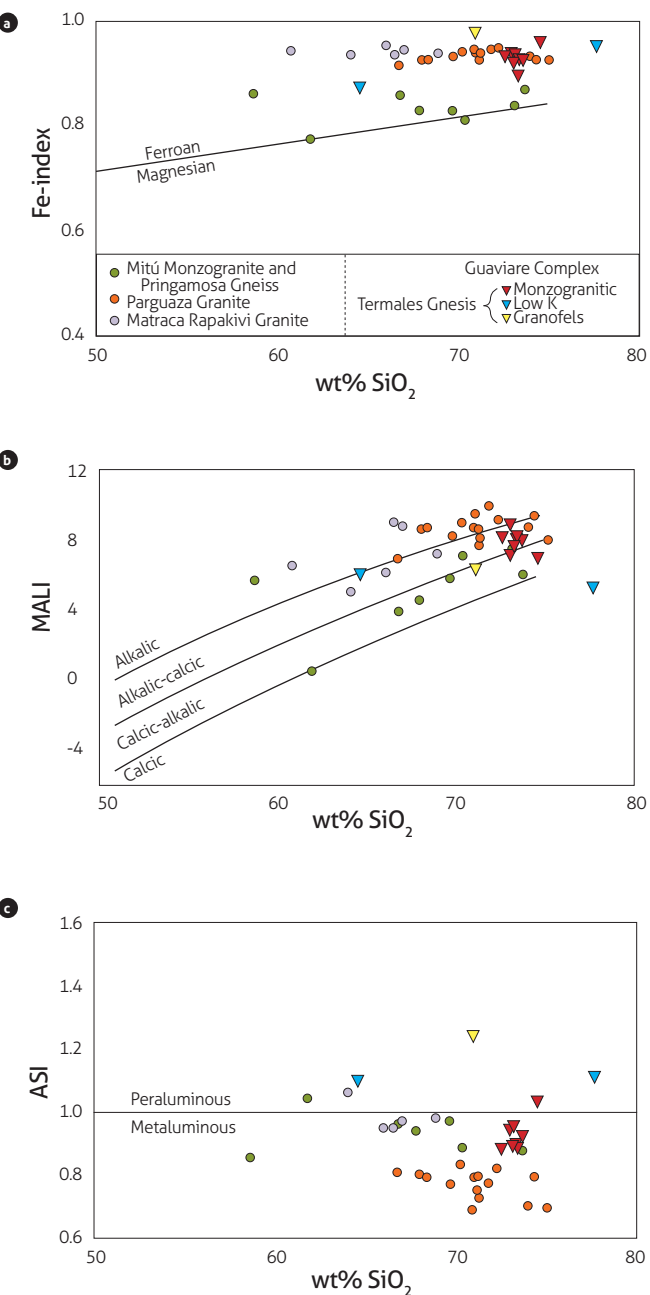
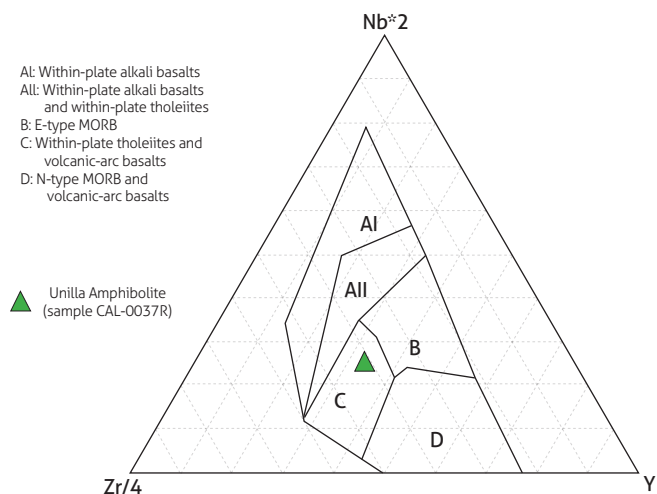


Figure 7. Classification diagrams of ferrous granitoid rocks (type A) (Frost and Frost, 2011) of protoliths of the Termalas Gneiss and of rocks of the Mitú Migmatite Complex by Rodríguez et al. (2011b), of the Parguaza Granite by Bonilla et al. (2013), and of the Matraca Rapakivi Granite by Bonilla et al. (2016).

The classification diagrams of Frost and Frost (2011) show that the samples from the Mitú Migmatitic Complex (Mitú Monzogranite and Pringamosa Gneiss) are mainly part of the field of metaluminous calc-alkaline granitoids, which indicates formation processes different from those of the rock suite of the Guaviare Complex. In turn, the protolith of the Termales Gneiss is more similar to the rocks of the Parguaza Granite (Figure 7), which are also of Mesoproterozoic age and which are alkaline and calc-alkaline metaluminous ferrous granites (Bonilla et al., 2013).

In the  $\text{Y}_\text{N}$ -vs.- $(\text{La}/\text{Y})_\text{N}$  diagram (Figure 9), the rocks of the Termales Gneiss are at an intermediate point between two



**Figure 8.** Nb-Zr-Y tectonic discrimination diagram (Meschede, 1986) of the Unilla Amphibolite. MORB: mid-ocean ridge basalts

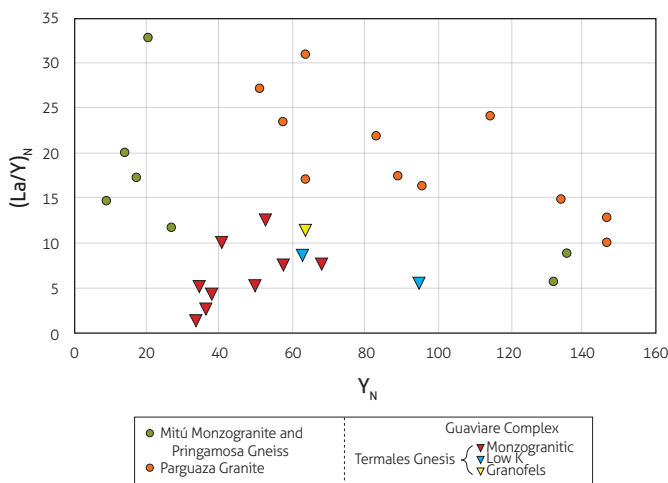


**Figure 9.**  $\text{Y}_\text{N}$ -vs.- $(\text{La}/\text{Y})_\text{N}$  diagram of rocks of the Guaviare Complex and Mitú Migmatitic Complex

extreme REE compositions of the Mitú Migmatite Complex and have lower values than those reported for the Parguaza Granite. The Mitú Migmatite Complex values suggest that these samples comprise different groups and that the rocks of the Guaviare Complex and those of the southern section of the geochronological province of Rio Negro-Juruena (Vaupés Belt) resulted from different formation processes.

#### 4.4 Isotopes

The results from the Sm-Nd and Sr isotope analysis of a sample of gneiss with biotite and hornblende (OPP-0042RA), from the main geochemical group, and of a sample of amphibolite (CAL-0037R) are outlined in Table 1. Based on the geochronological data (Annex 3), magmatic crystallization ages of 1312 and 1313 Ma (see section 4.4) were used to calculate the  $\varepsilon_{\text{Nd}}(\text{T})$  and the initial  $^{87}\text{Sr}/^{86}\text{Sr}$  ratio of the gneiss and amphibolite, respectively.

Both samples have slightly positive values of  $\varepsilon_{\text{Nd}}(\text{T})$  of +0.1 and +1.5, respectively, with  $T_{\text{DM}}$  model ages of 1810 and 1590 Ma (Figure 10). The initial  $^{87}\text{Sr}/^{86}\text{Sr}$  ratios of 0.7086 and 0.6427 are quite different from those of most known isotopic reservoirs, particularly the mantle. These initial  $^{87}\text{Sr}/^{86}\text{Sr}$  ratios likely reflect a Rb-Sr isotopic system imbalance, which commonly occurs due to the highly mobile character of Rb; some of this element may have been locally remobilized during metamorphism due to the action of interstitial or hydrothermal metamorphic fluids.

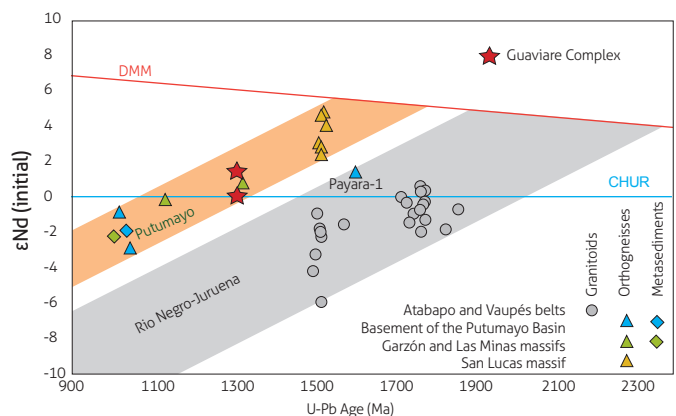


**Figure 10.**  $\varepsilon_{\text{Nd}}(\text{initial})$ -vs.-age plot comparing the new results of the Guaviare Complex with previously determined values for the Atabapo and Vaupés belts (Corradi et al., 2016), the basement of the Putumayo basin (Ibáñez Mejía et al., 2015), and the Garzón, Las Minas (Ibáñez Mejía et al., 2015), and San Lucas massifs (Cuadros et al., 2014)

The Nd isotopic composition of the Guaviare Complex suggests that this litho-demic unit has no affinity to the exposed basement of the Rio Negro-Juruena province, instead showing higher affinity to the lithospheric domain involved in the Putumayo Orogen. Depleted MORB mantle (DMM) curve according to the model by DePaolo (1981).

#### 4.5 Geochronology

Three samples (Table 2, Figure 2, Annex 3) of the Guaviare Complex were selected for analysis by LA ICP-MS Zircon U-Pb dating. The resulting data correspond to the crystallization ages of the igneous protoliths of the Termas Gneiss and Unilla Amphibolite and to the ages of the detritic zircons included in the sediments that form La Rompida Quartzite (Figure 11). Although some of the zircons, both igneous and detritic, show seemingly thin edges of metamorphic overgrowth or recrystallization, they could not be dated because they are signifi-

cantly smaller than the analytical spot used, so the metamorphism age could not be accurately determined. The absence of clear edges of thicker metamorphic overgrowth may be due to the degree of metamorphism of the rocks. As mentioned in the petrography, the quartzite was formed in green schist or low-amphibolite facies and the gneisses and amphibolite in low- or high-amphibolite facies, without being able to define it as one or the other. According to Rubatto (2017), green schist or low amphibolite facies do not commonly form metamorphic overgrowths.

**Table 1.** Sm-Nd and Sr isotopic data of the Termas Gneiss and Unilla Amphibolite

Sample	Sm (ppm)	Nd (ppm)	$^{143}\text{Nd}/^{144}\text{Nd}$	$^{147}\text{Sm}/^{144}\text{Nd}$	$\epsilon_{\text{Nd}}$ (T)	$T_{\text{DM}}$ (Ga)	Rb (ppm)	Sr (ppm)	$^{87}\text{Sr}/^{86}\text{Sr}$	$^{87}\text{Rb}/^{86}\text{Sr}$	$^{87}\text{Sr}/^{86}\text{Sr}_i$	T (Ga)	Lithological unit
OPP-0042RA	7.86	41.53	0.512005 ( $\pm 10$ )	0.1144	+1.5	1.59	317.0	45.0	1.03156 ( $\pm 8$ )	21.08454	0.64267	1.312	Termas Gneiss
CAL-0037R	11.65	51.62	0.512123 ( $\pm 15$ )	0.1365	+0.1	1.81	95.1	218.0	0.73200 ( $\pm 1$ )	1.26871	0.70858	1.313	Unilla Amphibolite

The uncertainties in the last two digits of the  $^{143}\text{Nd}/^{144}\text{Nd}$  ratios and in the last digit of the  $^{87}\text{Sr}/^{86}\text{Sr}$  ratio are  $2\sigma$ . The values of the  $^{143}\text{Nd}/^{144}\text{Nd}_{\text{CHUR}}$  and  $^{147}\text{Sm}/^{144}\text{Nd}_{\text{CHUR}}$  ratios used in the current calculations were 0.512630 and 0.1960, respectively (Bouvier et al., 2008).  $T_{\text{DM}}$  model ages according to the impoverished mantle model by DePaolo (1981). The concentrations of Rb and Sr were assessed by ICP-MS (Annex 1). The  $^{87}\text{Rb}/^{86}\text{Sr}$  ratio was calculated according to the procedure described by Faure and Mensing (2005)

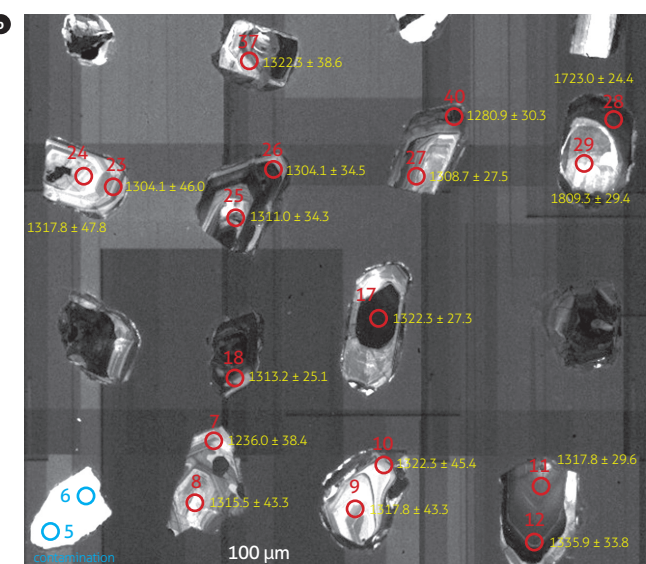
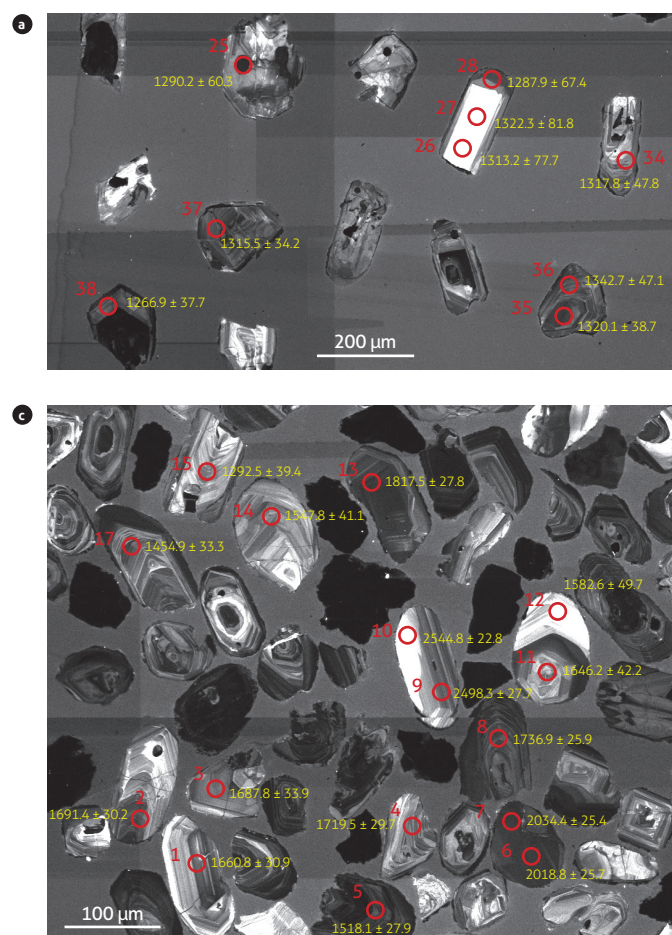


**Figure 11.** Cathodoluminescence images of zircons analyzed by LA-ICP-MS in the Guaviare Complex  
a) Termas Gneiss (OPP-0013RC). b) Unilla Amphibolite (CAL-0037R). c) La Rompida Quartzite (OPP-0036R)

**Table 2.** Samples with U-Pb geochronology analysis of the Guaviare Complex

Sample	IGM	North	East	Age $^{207}\text{Pb}/^{206}\text{Pb}$ (Ma)	main U-Pb peaks (Ma)	Method	Lithological unit
OPP-0013RC	5075619	740 964	1 132 115	$1312 \pm 5/11$		U-Pb Zircon	Termales Gneiss
CAL-0037R	5075337	727 157	1 137 003	$1313 \pm 8/12$		U-Pb Zircon	Unilla Amphibolite
OPP-0036R	5075642	738 681	1 130 738	Between $1238.4 \pm 74.4$ and $2849.7 \pm 28.9$	1300, 1500, 1730, 2010, 2680	U-Pb Zircon	La Rompida Quartzite

#### 4.5.1 Termales Gneiss (OPP-0013RC)

The study zircons show subhedral to euhedral shapes and a prismatic and bipyramidal habit, sometimes with radial fractures, and others are metamict (Figure 11a, Annex 4). They mostly

present well-marked, fine, oscillatory igneous zoning, although a few have patchy textures, which according to Corfu et al. (2003) are commonly found in rocks under relatively high pressure. Some zircons have inherited nuclei that may represent xenocrystals; others have thin edges of metamorphic overgrowth.

Most analyses indicated an age of approximately 1.3 Ga (Figure 12a), whereas a few others presented seemingly younger ages, due to either Pb loss or partial recrystallization. The matching analyses, illustrated in a Wetherill concordia diagram in Figure 12b, yielded a weighted mean  $^{206}\text{Pb}^*/^{207}\text{Pb}^*$  age =  $1.312 \pm 5/11$  ( $2\sigma$ ,  $n=66$ , MSWD = 1.3) (Figure 13), which is considered the age of crystallization of the igneous protolith during the Middle Mesoproterozoic (Ectasian).

The dated sample OPP-0013RC could be considered a member of the main group of gneisses described above based on geochemistry considering its similarities in modal mineralogical composition with the other gneisses of this group. As discussed below, the youngest age peak of La Rompida Quartzite, approximately 1.3 Ga, allows us to assume that most igneous protoliths in the area are close to that age, although it cannot rule out that the ages of low-K rocks, and even granofels, are somewhat different.

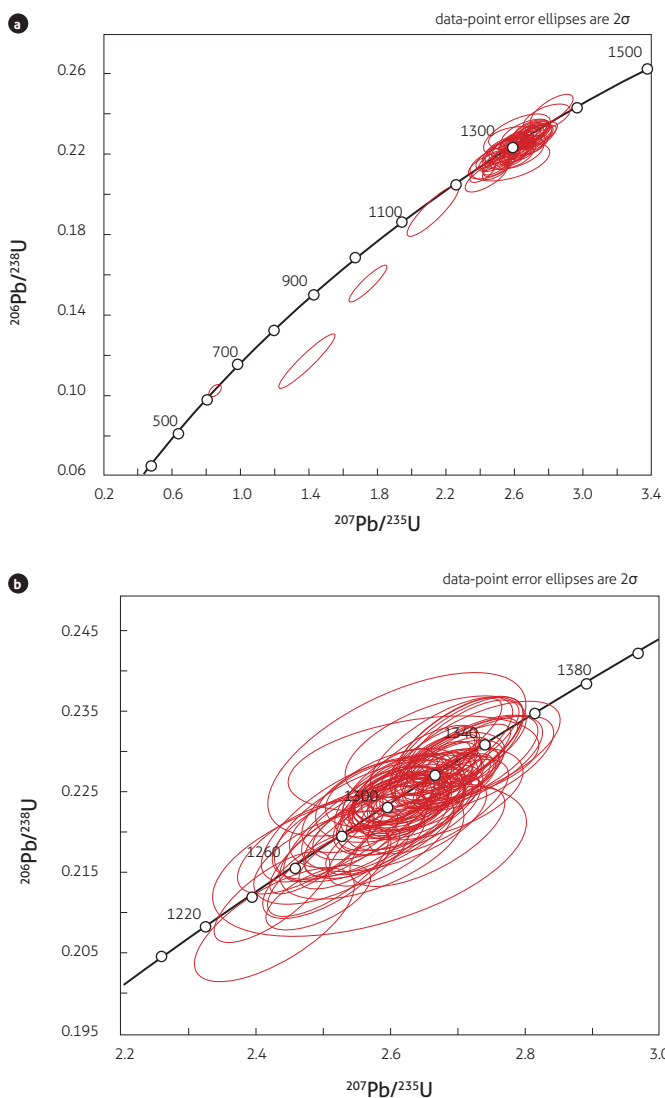


**Figure 12.** Wetherill concordia curve of the Termales Gneiss. Sample OPP-0013RC  
a) All zircons. b) Igneous ages of the sample protolith.

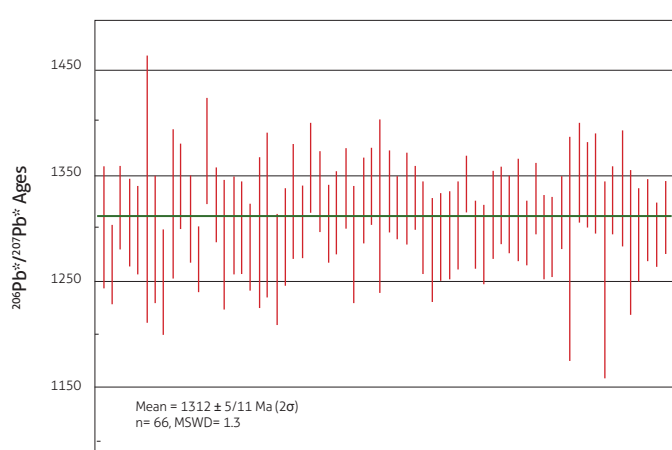


**Figure 13.** Mean  $^{206}\text{Pb}^*/^{207}\text{Pb}^*$  age of the sample from the Termales Gneiss. Sample OPP-0013RC

#### 4.5.2 Unilla Amphibolite (CAL-0037R)

The zircons collected from the Unilla Amphibolite are euhedral and prismatic, with fine to thick, oscillatory, igneous zoning and thin dark edges, which could be considered to have formed by metamorphism (Figure 11b, Annex 5). The vast majority of the analyses corroborated each other's findings (Figure 14a), and the spots located in nuclei with oscillatory zoning (as shown in Figure 14b) resulted in a weighted mean  $^{206}\text{Pb}^*/^{207}\text{Pb}^*$  age =  $1313 \pm 8/12$  ( $2\sigma$ ,  $n=19$ , MSWD = 0.9) (Figure 15). This age, interpreted as the age of crystallization of the igneous protolith of this amphibolite during the Middle Mesoproterozoic (Ectasian), is indistinguishable, within analytical uncertainties, from the age of crystallization assessed for the Termales Gneiss.

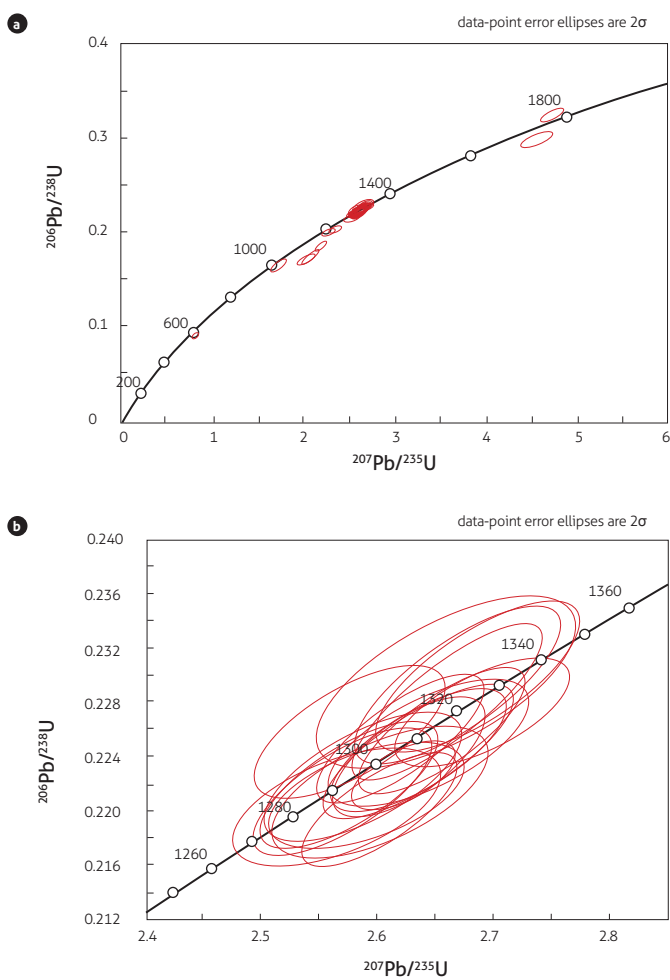


Figure 14. Wetherill concordia curve of the Unilla Amphibolite; Sample CAL-0037R  
a) All zircons. b) Igneous ages of the sample protolith.

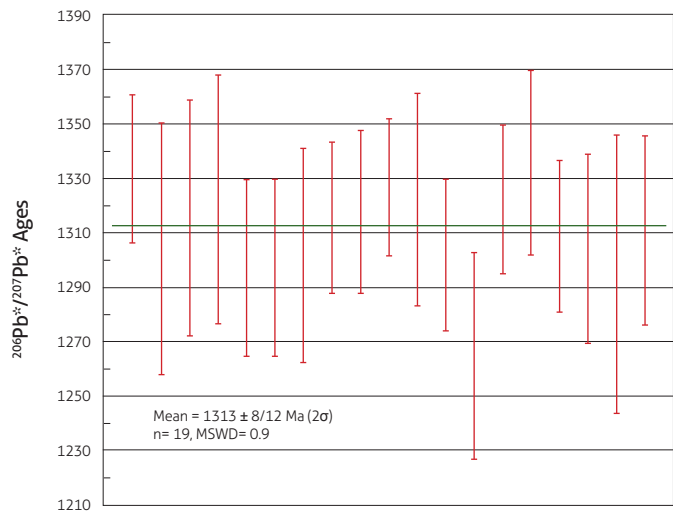


Figure 15. Mean  $^{206}\text{Pb}^*/^{207}\text{Pb}^*$  age of the CAL-0037R sample from the Unilla Amphibolite

Two inherited zircon xenocrystals resulted in apparent  $^{206}\text{Pb}/^{207}\text{Pb}$  ages of approximately 1.7-1.8 Ga, which indicates the assimilation of Paleoproterozoic materials, either at the source of the magmas or during the rise/eruption of the basaltic protoliths of this amphibolite. These ages match those indicated by Cordani et al. (2016) for the Atabapo Belt. Other, younger ages recorded in the zircons, between 607 and 1224 Ma, likely correspond to recrystallization or partial loss of Pb.

#### 4.5.3 La Rompida Quartzite (OPP-0036R)

The zircons in this sample are fractured and detrital, with shapes ranging from rounded to subangular, some from euhedral to subhedral, and with a prismatic and bipyramidal habit, which indicates variation in the input sources. The vast majority of them present fine oscillatory igneous zoning (Figure 11c, Annex 6); only some crystals have a thin edge, which may correspond to metamorphic growth. A few crystals have more complex zoning similar to sector zoning (Corfu et al., 2003), possibly due to metamorphic events.

The analytical results, illustrated in a Wetherill concordia plot (Figure 16a), show that most analyses indicated individual  $^{206}\text{Pb}/^{207}\text{Pb}$  ages ranging from  $1238 \pm 74$  Ma (youngest age) to  $2850 \pm 29$  Ma (oldest age). The main distribution peaks are located at approximately 1300, 1500, 1730, 2010, and 2680 Ma (Figure 16b), with the main peak at 1730 Ma, followed by the peak at 1500 Ma. The  $^{206}\text{Pb}/^{207}\text{Pb}$  ages older than 1829 Ma were

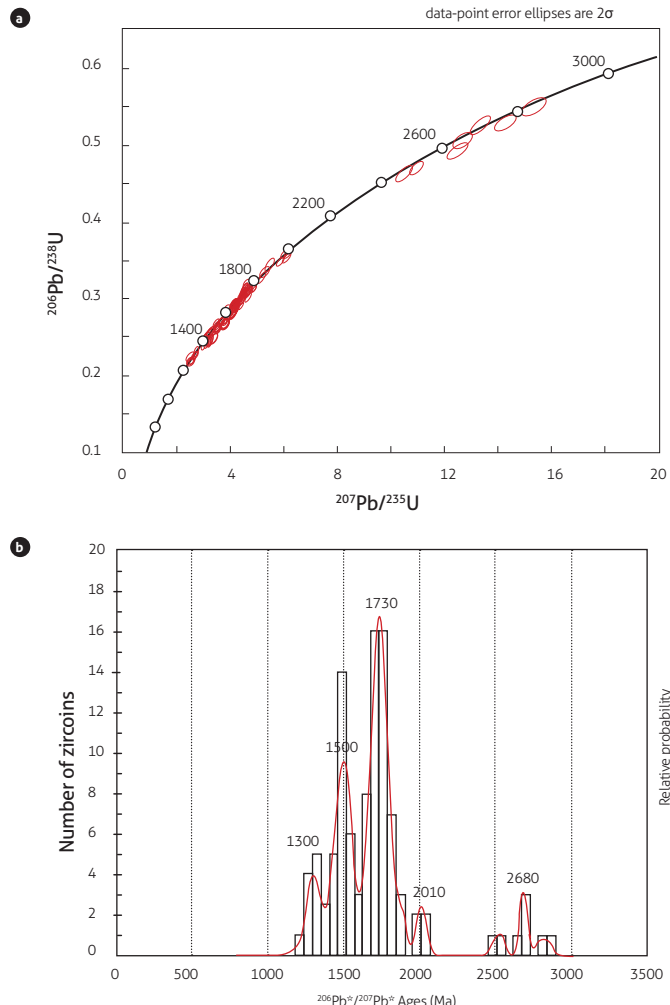


**Figure 16.** La Rompida Quartzite; OPP-0036R sample  
 a) Wetherill concordia curve. b) Probability plot of the  $^{206}\text{Pb}/^{207}\text{Pb}$  ages of dendritic zircons showing the maximum age distribution peaks.

assessed in rounded grains, whereas the oldest  $^{206}\text{Pb}/^{207}\text{Pb}$  age of the euhedral grains was 1827.2 Ma.

## 5. DISCUSSION

The geochemical patterns and the geochronological ages assessed for rocks from the Termalas Gneiss and the Unilla Amphibolite indicate that a primarily bimodal magmatism, mostly with a ferrous calc-alkaline granitic (type A) and, at a smaller volume, mafic composition occurred in the extreme NW of the Amazonian Craton at 1.3 Ga (Figures 13 and 15), in the Ectasic period of the Mesoproterozoic. This magmatism could be related to extensional environments, to the formation of rifts

over long periods, or to a Mesoproterozoic extensional arc whose tectonic regime may have resulted in the opening of a back-arc basin ca. 1.3 Ga.

In addition, evidence of a more peraluminous, calc-alkaline, granitic magmatism indicates variations in magmatic processes, which could be related to changes in mantle and crustal inputs over time.

Magmatism from ca. 1.3 Ga had not yet been discovered in outcrops of the Amazonian Craton in eastern Colombia. The findings of this study clearly document the existence of this bimodal magmatism in the NW reaches of the Craton, represented by the crystallization ages assessed in igneous protoliths of the Guaviare Complex. The magmatism ages overlap with the beginning of the intraplate heating of the Nickerian event in the northern section the Amazon Craton (Cordani et al., 2016). Near the NW edge of the Amazonian Craton, Ibáñez Mejía et al. (2011) documented the existence of magmatism dated between 1.3 and 1.2 Ga, recorded in igneous protoliths from the Garzón and Las Minas massifs.

In the Proterozoic, from 1800 to 1300 Ma, the magmatism of ferrous granites (type A) were apparently quite common in the NW of the Amazonian Craton because each of the granitic protoliths of Termalas Gneiss, the Parguaza Granite (Gaudette et al., 1978; Bonilla et al., 2013), the Matracá Granite (Bonilla et al., 2016), and the granitic protoliths of the Mitú Migmatite Complex (Rodríguez et al., 2011a, 2011b) have these compositions (Figure 7).

Regarding the ages assessed for the quartzites (Figure 16b), the youngest peak, at 1300 Ma, marks the maximum age of deposition of its sedimentary protolith and is close to the igneous ages of the gneisses and amphibolites of the Guaviare Complex. Given this similarity, these rocks—or other units of similar age in the region—may have contributed detrital material to nearby sedimentary basins, thereby forming the protoliths of La Rompida Quartzite during the Ectasic or later. The peak at approximately 1500 Ma is in line with the magmatism found in the Vaupés Belt and in Caquetá (Araracuara), and the main peak at approximately 1730 Ma matches the ages of the Atabapo Belt (Cordani et al., 2016), which clearly shows that the basin where the sedimentary protolith of La Rompida Quartzite was formed received detrital from the interior of the craton derived from those belts.

The peak at 2680 Ma, corresponding to the Neoarchean, matches the dates present in the Central Amazonian province, which would indicate that the current area of Guaviare was

bathed by rivers that either were born in the core of the Amazonian Craton or that drained ancient sedimentary rocks that had been formed with contributions from the core of the craton. Zircons older than 1829 Ma have good roundness, indicating good transport conditions. The detrital zircons of those ages are very scarce in the dates assessed so far in the Colombian part of the Amazonian Craton. Cordani et al. (2016) reported no Archean zircons, whereas Ibáñez Mejía et al. (2011) reported scarce inherited zircons aged approximately 2.5 Ga when dating samples from the Vaupés and Apaporis rivers.

The basin most likely also received sedimentary contributions from the craton, in contrast to most metasedimentary units known to date of the Putumayo Orogen, in which no magmatic events derived from the craton were recorded between 1.59 and 1.01 Ga (Ibáñez Mejía et al., 2011). This situation could be explained if the current area of the Guaviare were over or immediately adjacent to the craton, whereas the Putumayo Orogen would have been formed some distance from the craton, where the sediments derived from this craton did not reach.

From the late Mesoproterozoic to the early Neoproterozoic, during the formation of the supercontinent Rodinia, the Mirovoi Ocean was completely consumed, and the continents Laurentia, Amazonia, and Baltica collided, which generated orogenies in the different blocks (Cawood and Pisarevsky, 2017). The Laurentia collision with the western section of the Amazonia formed the Grenvillian Orogeny in Laurentia and the Sunsás Orogeny in Amazonia (Ibáñez Mejía et al., 2011). The collision between the northwestern part of Amazonia and the southern edge of Baltica produced the Putumayo Orogen in Amazonia, the Zapotec Orogeny in the Oaxaquia block—currently part of Mexico—and the Sueconoruega Orogeny in southern Scandinavia (Weber and Schulze, 2014; Ibáñez Mejía et al., 2011, 2015; Cawood and Pisarevsky, 2017).

After 1.28 Ga, which is age of the youngest detrital zircons, but before the Ediacaran, a period during which the rocks of the San José del Guaviare Nepheline Syenites were intruded (Maya et al., 2018), the igneous and sedimentary protoliths of the Guaviare Complex underwent regional metamorphism over a length of time still undetermined because the metamorphic event recorded in the rocks produced only small overheating edges in the zircons, which could not be dated. Two Proterozoic metamorphic events younger than 1.28 Ga are known in the Colombian section of the Amazonian Craton: one from 1.05 to 1.01 Ga and another ca. 0.99 Ga (Ibáñez Mejía et al.,

2011). Therefore, the regional metamorphism that affected the basement of the Guaviare Complex likely occurred during one of these Putumayo Orogenic events. However, the possibility that this was an independent event cannot be ruled out.

The difference in age between the Guaviare Complex (~1.3 Ga) and Vaupés Belt (~1.58 to 1.52 Ga) indicates that both groups of rocks were formed at different times. Based on the Nd isotopic data (Table 1 and Figure 10), the igneous protoliths of the rocks from the Guaviare Complex likely derive from the partial fusion of rocks belonging to the same lithospheric segment (which would probably correspond to an underplate of mafic rocks at the base of the crust), which gave rise to the precursor magmas of the protoliths of the gneisses, amphibolites, and granulites of the San Lucas mountain range (Cuadros et al., 2014). Considering that the gneisses and amphibolites of the San Lucas mountain range have  $T_{DM}$  ages ranging from 1.5 to 1.8 Ga (Cuadros et al., 2014), the oldest zircons, with ages of 1.7-1.8 Ga, found in the Unilla Amphibolite may have been inherited from that common source consisting of juvenile rocks of this age, though it cannot rule out the possibility that such zircons represent, conversely, xenocrystals added by assimilation of wall rocks during the emplacement of magmas. In the above scenario, the slightly positive  $\epsilon_{Nd}$  values of the rocks from the Guaviare Complex could be explained without the need to invoke a high degree of assimilation of additional crustal material because the mantle rocks derived from the underplate would have ~1.3-Ga Nd isotopic ratios, in line with those found in the gneiss and amphibolite samples (Figure 10).

Another possibility is that the precursor magmas of the Guaviare Complex protoliths are juvenile and were directly derived from impoverished mantle (which, at ~1.3 Ga, would have  $\epsilon_{Nd}$  values near +6), after which they underwent contamination with less radiogenic crustal material that had markedly negative  $\epsilon_{Nd}$  values, which would have resulted in hybrid magmas with the observed values of  $\epsilon_{Nd}$  ranging from 0 to +1.5. If this is true, two questions arise: 1) Had such contamination occurred at the source or during the emplacement of the magmas? 2) What crust was responsible for the contamination? More data are needed to answer these questions. Importantly, for example, the rocks from the Atabapo and Vaupés Belts, of the Rio Negro-Juruena province (Cordani et al., 2016), would have, at ~1.3 Ga old,  $\epsilon_{Nd}$  values negative enough to be considered possible outliers in the origin of the protoliths of the rocks from the Guaviare Complex, through contamination of juvenile magma.

## 6. CONCLUSIONS

In the department of Guaviare, the Proterozoic metamorphic rocks are represented by granitic orthogneisses and granofels, amphibolites, and muscovite quartzites, which together form the Guaviare Complex. The Guaviare Complex is a new Proterozoic unit of crystalline basement located in southeastern Colombia that crops out in an intermediate position between known Precambrian rock locations in Colombia, with the Amazonian Craton (Atabapo and Vaupés belts) to the east and El Garzón Complex to the west. The rocks of the Guaviare Complex are divided into three lithological units termed Termalas Gneiss, Unilla Amphibolite, and La Rompida Quartzite, which were characterized in Plate 372 – El Retorno during the geologic mapping conducted by Serviminas and the SGC. The gneissic metamorphic rocks described in the Plate 371 - Puerto Cachicamo are also included in this complex.

The protoliths of the metamorphic rocks of the Guaviare Complex indicate magmatism of ferrous granitoids (type A) of monzogranitic and tonalitic-quartzdioritic composition and a mafic magmatism of gabbroic composition. This magmatism would have been part of an orogeny after which the granites were exposed by erosion, subsequently producing sediments that incorporated materials both from the granite and from distant areas of the craton. These psammitic, quartzarenitic, and arkosic sediments, with pelitic content, underwent regional metamorphism of half a degree in amphibolite facies, although this regional metamorphism could have been partly of a low degree, in green schist facies for the quartzite. Some of these rocks present a dynamic component superimposed on regional metamorphism.

The zircon U-Pb ages assessed for the igneous protoliths of the rocks from the Guaviare Complex are  $1312 \pm 5/11$  Ma for the Termalas Gneiss and  $1313 \pm 8/12$  Ma for the Unilla Amphibolite. In La Rompida Quartzite, the youngest detrital age is  $1238 \pm 74$  Ma, and the oldest age is  $2850 \pm 29$  Ma, with main peaks of 1300, 1500, 1730, 2010, and 2680 Ma. This metasedimentary unit, whose deposition occurred in the Ectasian or later, does not seem to have known equivalents in the Colombian Amazonian Craton.

The metamorphism age is not yet known with precision, and it ranges from 1.3 to 0.6 Ga. Given the regional geology of the NW of the Amazonian Craton, this metamorphism is likely related to the Putumayo province, coming either with the event recorded between 1.05 and 1.01 Ga or with the event

closer to 0.99 Ga. However, the possibility that a different, perhaps slightly older, metamorphic event occurred cannot be ruled out.

The chemical characteristics of the metaigneous rocks of the Guaviare Complex, Termalas Gneiss and Unilla Amphibolite, suggest that most of the rocks originated as part of a bimodal magmatism formed in an extensional environment associated with a backarc basin. The source of the magmatism, dated at 1.3 Ga, could comprise the mixture between mantle material that is possibly differentiated and older, continental, “inherited” material that was reworked during the Ectasian. The Nd isotopic ratios of the Termalas Gneiss and Unilla Amphibolite are in line with the above, so the above explanation is the preferred interpretation of this work, although the hypothesis that such isotopic ratios reflect an older and dominant mantle source, analogous to that responsible for the bimodal association of precursor magmas of basement rocks of the San Lucas mountain range, should not be completely ruled out.

## ACKNOWLEDGEMENTS

This study summarizes part of the results from the project entitled “*Elaboración de la cartografía geológica en un conjunto de planchas a escala 1:100.000 ubicadas en dos zonas del territorio colombiano, zona sur*” [“Preparation of the geologic map of a set of plates located in two areas of southern Colombia at a 1:100,000 scale”] of the Dirección de Geociencias Básicas of the Servicio Geológico Colombiano – SGC, developed by the Geology team of the company Serviminas under contract number 508 of 2017. We thank the SGC geologists and the Ingtec team for reading the manuscript and making recommendations, which allowed us to improve the geologic map and the explanatory memorandum of Plate 372 – El Retorno. Finally, the authors thank the anonymous reviewers for their recommendations, that helped to improve this article.

## SUPPLEMENTARY DATA

Supplementary data to this article can be found online at <https://doi.org/10.32685/0120-1425/boletingeo.47.2020.502>

## REFERENCES

- Bonilla, A., Frantz, J., Charão-Marques, J., Cramer, T., Franco, J., & Amaya, Z. (2016). Magmatismo rapakivi en la cuenca

- media del río Inírida, departamento de Guainía, Colombia. *Boletín de Geología*, 38(1), 17-32. <https://doi.org/10.18273/revbol.v38n1-2016001>
- Bonilla, A., Frantz, J., Charão-Marques, J., Cramer, T., Franco, J., Mulcher, E., & Amaya, Z. (2013). Petrografía, geoquímica y geocronología del Granito de Parguaza en Colombia. *Boletín de Geología*, 35(2), 83-104.
- Bonin, B. (2007). A-type granites and related rocks: evolution of a concept, problems and prospects. *Lithos*, 97(1-2), 1-29. <https://doi.org/10.1016/j.lithos.2006.12.007>
- Bouvier, A., Vervoort, J., & Patchett, P. (2008). The Lu-Hf and Sm-Nd isotopic composition of CHUR: Constraints from unequilibrated chondrites and implications for the bulk composition of terrestrial planets. *Earth and Planetary Science Letters*, 273(1-2), 48-57. <https://doi.org/10.1016/j.epsl.2008.06.010>
- Bowie, S., & Simpson, P. (1977). Microscopy: reflected light. In J. Zussman (ed.), *Physical methods in determinative mineralogy* (2nd ed., pp. 109-165). Academic Press, Ltd.
- Buchely, F., Gómez, L., Reyes Abril, J., Buitrago, J., Ibáñez, R., Tovar, A., Velasco, D., Berg, T., Nota, L., Culebra, D., Beceerra, L., Silveira, B., Valencia, D., & Arias, O. (2015). *Geología de la plancha 371 - Puerto Cachicamo. Memoria explicativa. Escala 1: 100.000*. Servicio Geológico Colombiano.
- Caicedo, J. C. (2003). *Toma de datos en la libreta de campo. Ingeominas*.
- Cawood, P., & Pisarevsky, S. (2017). Laurentia-Baltica-Amazonia relations during Rodinia assembly. *Precambrian Research*, 292, 386-397. <https://doi.org/10.1016/j.precamres.2017.01.031>
- Cordani, U., Cardona, A., Jimenez, D., Liu, D., & Nutman, A. (2005). Geochronology of proterozoic basement inliers in the Colombian Andes: tectonic history of remnants of a fragmented Grenville belt. *Geological Society of London, Special Publications*, 246, 329-346. <https://doi.org/10.1144/GSL.SP.2005.246.01.13>
- Cordani, U., Sato, K., Sproessner, W., & Fernandes, F. (2016). U-Pb zircon ages of rocks from the Amazonas territory of Colombia and their bearing on the tectonic history of the NW sector of the Amazonian Craton. *Brazilian Journal of Geology*, 46, 5-35. <https://doi.org/10.1590/2317-4889201620150012>
- Cordani, U., Tassinari, C., Teixeira, W., Kawashita, K., & Basei, M. (1979). *Evolução tectônica da Amazônia com base nos dados geocronológicos. Actas II. Congreso Geológico Chileno*.
- Corfu, F., Hanchar, J., Hoskin, P., & Kinny, P. (2003). Atlas of zircon textures. *Reviews in Mineralogy and Geochemistry*, 53(1), 469-500. <https://doi.org/10.2113/0530469>
- Cox, K., Bell, J., & Pankhurst, R. (1979). *The interpretation of igneous rocks* (First). Springer Science & Business Media. <https://doi.org/10.1007/978-94-017-3373-1>
- Cuadros, F., Botelho, N., Ordóñez-Carmona, O., & Matteini, M. (2014). Mesoproterozoic crust in the San Lucas Range (Colombia): An insight into the crustal evolution of the northern Andes. *Precambrian Research*, 245, 186-206. <https://doi.org/10.1016/j.precamres.2014.02.010>
- DePaolo, D. (1981). A neodymium and strontium isotopic study of the mesozoic calc-alkaline granitic batholiths of the Sierra Nevada and Peninsular Ranges, California. *Journal of Geophysical Research*, 86(B11), 10470-10488. <https://doi.org/http://dx.doi.org/10.1029/JB086iB11p10470>
- Faure, G., & Mensing, T. (2005). *Isotopes: principles and applications* (Third). John Wiley & Sons, Inc.
- Frost, C., & Frost, B. (2011). On ferroan (A-type) granitoids: their compositional variability and modes of origin. *Journal of Petrology*, 52(1), 39-53. <https://doi.org/10.1093/petrology/egq070>
- Galvis, J., Huguett, A., & Ruge, P. (1979). Geología de la Amazonia Colombiana. Informe No. 1792. *Boletín Geológico*, 22(3), 1-153.
- Gaudette, H., Mendoza, V., Hurley, P., & Fairbairn, H. (1978). Geology and age of the Parguaza Rapakivi Granite, Venezuela. *Geological Society of America Bulletin*, 89(9), 1335-1340. [https://doi.org/10.1130/0016-7606\(1978\)89<1335:GAAOTP>2.0.CO;2](https://doi.org/10.1130/0016-7606(1978)89<1335:GAAOTP>2.0.CO;2)
- Gehrels, G., Valencia, V., & Ruiz, J. (2008). Enhanced precision, accuracy, efficiency, and spatial resolution of U-Pb ages by laser ablation-multicollector-inductively coupled plasma-mass spectrometry. *Geochemistry, Geophysics, Geosystems*, 9(3), 1-13. <https://doi.org/10.1029/2007GC001805>
- Gioia, S., Hollanda, M., & Pimentel, M. (1999). *Uso de resinas RE-Spec e Sr-Spec em geoquímica isotópica. En Anais do V congresso de geoquímica dos países de língua portuguesa e VII Congresso Brasileiro de Geoquímica*. 218.
- Gioia, S., & Pimentel, M. (2000). The Sm-Nd isotopic method in the geochronology laboratory of the University of Brasília. *Anais da Academia Brasileira de Ciencias*, 72(2), 219-245. <https://doi.org/10.1590/s0001-37652000000200009>
- Heinrich, E. (1965). *Microscopic identification of minerals*. McGraw-Hill.

- Ibañez-Mejía, M., Bloch, E., & Vervoort, J. (2018). Timescales of collisional metamorphism from Sm-Nd, Lu-Hf and U-Pb thermochronology: a case from the Proterozoic Putumayo Orogen of Amazonia. *Geochimica et Cosmochimica Acta*, 235, 103-126. <https://doi.org/10.1016/j.gca.2018.05.017>
- Ibañez-Mejía, M., & Cordani, U. G. (2020). Zircon U-Pb geochronology and Hf-Nd-O isotope geochemistry of the Paleo- to Mesoproterozoic basement in the westernmost Guiana Shield. In: Gómez, J. & Mateus-Zabala, D. (eds.), *The Geology of Colombia, Volume 1 Proterozoic – Paleozoic*. Publicaciones Geológicas Especiales 35. Servicio Geológico Colombiano. <https://doi.org/10.32685/pub.esp.35.2019.04>
- Ibáñez-Mejía, M., Pullen, A., Arenstein, J., Gehrels, G., Valley, J., Ducea, M., Mora, A., Pecha, M., & Ruiz, J. (2015). Unraveling crustal growth and reworking processes in complex zircons from orogenic lower-crust: the proterozoic Putumayo Orogen of Amazonia. *Precambrian Research*, 267, 285-310. <https://doi.org/10.1016/j.precamres.2015.06.014>
- Ibáñez-Mejía, M., Ruiz, J., Valencia, V., Cardona, A., Gehrels, G., & Mora, A. (2011). The Putumayo Orogen of Amazonia and its implications for Rodinia reconstructions: new U-Pb geochronological insights into the proterozoic tectonic evolution of northwestern South America. *Precambrian Research*, 191(1-2), 58-77. <https://doi.org/10.1016/j.precamres.2011.09.005>
- Ibáñez-Mejía, M., & Tissot, F. (2019). Extreme Zr stable isotope fractionation during magmatic fractional crystallization. *Science Advances*, 5(12), 1-14. <https://doi.org/10.1126/sciadv.aax8648>
- López, J., Khurama, S., Bernal, L., & Cuellar, M. (2007). *El Complejo Mitú: una nueva perspectiva*. Memorias XI Congreso Colombiano de Geología. 1-16.
- Lugmair, G., & Martí, K. (1978). Lunar initial  $^{143}\text{Nd}/^{144}\text{Nd}$ : differential evolution of the lunar crust and mantle. *Earth and Planetary Science Letters*, 39(3), 349-357. [https://doi.org/10.1016/0012-821X\(78\)90021-3](https://doi.org/10.1016/0012-821X(78)90021-3)
- Maya, M., Amaya, C., Gómez, J., Tabares, G., Palacio, A., García, J., Tabares, F., Camacho, J., Betancur, J., & Duque, J. (2019). *Guía para la elaboración de la libreta de campo de un proyecto de cartografía geológica*. Serviminas.
- Maya, M., Amaya, C., Restrepo, J., Duque, J., Palacio, A., Gutiérrez, P., Pérez, O., Ríos, C., Arias, E., & Bedoya, J. (2018). *Memoria explicativa de la Plancha 372 – El Retorno*. Escala 1: 100.000. Servicio Geológico Colombiano.
- McDonough, W., & Sun, S. (1995). The composition of the earth. *Chemical Geology*, 120(3-4), 223-253. [https://doi.org/10.1016/0009-2541\(94\)00140-4](https://doi.org/10.1016/0009-2541(94)00140-4)
- McDonough, W., Sun, S., Ringwood, A., Jagoutz, E., & Hofmann, A. (1992). Potassium, rubidium, and cesium in the earth and moon and the evolution of the mantle of the earth. *Geochimica et Cosmochimica Acta*, 56(3), 1001-1012. [https://doi.org/10.1016/0016-7037\(92\)90043-I](https://doi.org/10.1016/0016-7037(92)90043-I)
- Meschede, M. (1986). A method of discriminating between different types of mid-ocean ridge basalts and continental tholeiites with the Nb-Zr-Y diagram. *Chemical Geology*, 56(3-4), 207-218. [https://doi.org/10.1016/0009-2541\(86\)90004-5](https://doi.org/10.1016/0009-2541(86)90004-5)
- Patiño-Douce, A. (1997). Generation of metaluminous A-type granites by low-pressure melting of calc-alkaline granitoids. *Geology*, 25(8), 743-746. [https://doi.org/10.1130/0091-7613\(1997\)025<0743:GOMATG>2.3.CO;2](https://doi.org/10.1130/0091-7613(1997)025<0743:GOMATG>2.3.CO;2)
- Pullen, A., Ibáñez-Mejía, M., Gehrels, G., Giesler, D., & Pecha, M. (2018). Optimization of a laser ablation-single collector-inductively coupled plasma-mass spectrometer (thermo element 2) for accurate, precise, and efficient zircon U-Th-Pb geochronology. *Geochemistry, Geophysics, Geosystems*, 19(10), 3689-3705. <https://doi.org/10.1029/2018GC007889>
- Rodríguez, G., Sepúlveda, J., Ramírez, C., Ortiz, F., Ramos, K., Bermúdez, J., & Sierra, M. (2011a). *Cartografía geológica y exploración geoquímica de la Plancha 443 Mitú. Memoria explicativa. Escala 1:100.000*. Ingeominas.
- Rodríguez, G., Sepúlveda, J., Ramírez, C., Ortiz, F., Ramos, K., Bermúdez, J., & Sierra, M. (2011b). *Unidades, petrografía y composición química del Complejo Migmatítico de Mitú. Boletín de Geología*, 33(1), 27-42.
- Rodríguez, G., Zapata, G., Velásquez, M., Cossio, U., & Londoño, A. (2003). *Geología de las Planchas 367 - Gigante, 368 - San Vicente del Caguán, 389 - Timaná, 390 - Puerto Rico, 391 - Lusitania (parte noroccidental) y 414 - El Doncello, departamentos de Caquetá y Huila. Memoria explicativa*. Ingeominas.
- Rubatto, D. (2017). Zircon: the metamorphic mineral. *Reviews in Mineralogy and Geochemistry*, 83(1), 261-295. <https://doi.org/10.2138/rmg.2017.83.9>
- Schmid, R., Fettes, D., Harte, B., Davis, E., & Desmons, J. (2007). *A systematic nomenclature for metamorphic rocks: 1. How to name a metamorphic rock. Recommendations by the IUGS Subcommission on the Systematics of Metamorphic Rocks: Web version 01/02/07*. 22.

- Skjerlie, K., & Johnston, A. (1993). Fluid-absent melting behavior of an F-rich tonalitic gneiss at mid-crustal pressures: implications for the generation of anorogenic granites. *Journal of Petrology*, 34(4), 785-815. <https://doi.org/10.1093/petrology/34.4.785>
- Sláma, J., Košler, J., Condon, D., Crowley, J., Gerdes, A., Hanchar, J., Horstwood, M., Morris, G., Nasdala, L., Norberg, N., Schaltegger, U., Schoene, B., Tubrett, M., & Whitehouse, M. (2008). Plešovice zircon - A new natural reference material for U-Pb and Hf isotopic microanalysis. *Chemical Geology*, 249(1-2), 1-35. <https://doi.org/10.1016/j.chemgeo.2007.11.005>
- Tassinari, C., & Macambira, M. (1999). Geochronological provinces of the Amazonian Craton. *Episodes*, 22(3), 174-182. <https://doi.org/10.18814/epiiugs/1999/v22i3/004>
- Weber, B., & Schulze, C. (2014). Early Mesoproterozoic (>1.4 Ga) ages from granulite basement inliers of SE Mexico and their implications on the Oaxaquia concept - evidence from U-Pb and Lu-Hf isotopes on zircon. *Revista Mexicana de Ciencias Geológicas*, 31(3), 377-394.
- Winkler, H. (1976). *Petrogenesis of metamorphic rocks* (fourth). Springer-Verlag.
- Winter, J. (2001). *An introduction to igneous and metamorphic petrology*. Prentice-Hall Inc.
- Whitney, D., & Evans, B. (2010). Abbreviations for names of rock-forming minerals. *American Mineralogist*, 95(1), 185-187. <https://doi.org/10.2138/am.2010.3371>

## SUPPLEMENTARY DATA

### ANNEX 1. GEOCHEMICAL DATA OF THE GUAVIARE COMPLEX

Sample	Termalas Gneiss										Unilla Amphibolite	
	Group 1					Group 2						
	CAL-0035RA	CAL-0036R	OPP-0004R	OPP-0013RB	OPP-0037R	OPP-0042RA	OPP-0046R	OPP-0200R	CMR-0041R	OPP-0013RA	OPP-0047R	CAL-0037R
IGM	5075334	5075336	5075606	5075618	5075643	5075648	5075653	5075696	5075415	5075617	5075654	5075337
Oxide (%)												
SiO <sub>2</sub>	73.12	73.37	72.97	74.56	73.23	72.61	73.41	73.65	64.59	71.00	77.62	51.01
TiO <sub>2</sub>	0.38	0.33	0.35	0.36	0.37	0.37	0.38	0.37	0.43	0.45	0.39	3.37
Al <sub>2</sub> O <sub>3</sub>	13.36	13.08	13.16	12.85	13.34	13.00	13.38	12.94	18.26	15.94	11.62	13.61
Fe <sub>2</sub> O <sub>3</sub>	3.52	2.74	3.42	2.87	3.43	3.49	3.47	3.52	3.75	2.65	3.38	16.01
MnO	0.10	0.05	0.04	0.02	0.06	0.07	0.06	0.07	0.11	0.02	0.05	0.24
MgO	0.31	0.32	0.23	0.12	0.24	0.25	0.27	0.29	0.54	0.06	0.17	3.36
CaO	1.57	0.90	0.29	0.85	0.91	0.92	1.07	0.80	2.97	1.47	1.12	7.14
Na <sub>2</sub> O	3.69	2.74	3.36	3.95	2.63	2.77	3.33	3.95	8.58	7.26	5.86	3.05
K <sub>2</sub> O	4.99	6.18	5.73	3.76	5.89	6.19	5.83	4.78	0.44	0.47	0.53	1.29
P <sub>2</sub> O <sub>5</sub>	0.06	0.06	0.05	0.05	0.05	0.04	0.05	0.05	0.05	0.03	0.05	0.57
Cr <sub>2</sub> O <sub>3</sub>	<0.01	<0.01	<0.01	<0.01	<0.01	<0.01	<0.01	<0.01	<0.01	<0.01	<0.01	<0.01
LOI	0.33	0.11	0.27	0.39	0.49	0.11	0.08	0.43	0.02	0.27	0.10	0.64
Total	101.43	99.88	99.87	99.78	100.64	99.82	101.33	100.85	99.74	99.62	100.89	100.29
Element (ppm)												
Ba	379.00	517.00	454.00	644.00	435.00	461.00	435.00	406.00	23.60	54.90	68.60	308.00
Rb	261.00	323.00	311.00	121.00	309.00	317.00	234.00	232.00	7.00	17.70	52.90	95.10
Sr	70.90	62.90	42.10	150.50	50.10	45.00	78.10	42.20	114.00	187.00	68.60	218.00
Cs	0.96	2.09	0.86	0.50	1.66	4.03	1.62	0.59	0.16	0.28	1.79	0.43
Ga	25.20	21.10	23.80	21.70	24.10	23.10	22.80	22.20	32.50	23.10	19.60	26.50
Ta	3.90	4.00	3.70	3.60	3.90	4.40	4.40	4.10	5.10	4.50	4.50	1.70
Nb	66.50	53.10	61.60	65.20	64.70	62.30	63.70	65.50	78.20	77.80	64.90	22.40
Hf	14.10	9.40	15.70	14.80	15.30	15.80	15.80	16.10	16.90	2.50	16.20	7.40
Zr	597.00	377.00	660.00	587.00	662.00	625.00	608.00	662.00	674.00	94.00	635.00	293.00
Y	107.00	54.20	63.90	82.50	52.80	56.50	78.40	90.40	148.50	99.80	98.30	60.00
Th	34.10	31.80	34.20	35.60	34.60	28.20	32.80	34.10	38.10	3.27	36.10	6.06
U	8.52	4.99	9.06	10.45	9.38	5.40	5.09	9.69	11.65	3.20	8.96	1.36
Cr	<10	10.00	10.00	10.00	<10	40.00	40.00	10.00	40.00	40.00	40.00	40.00
Ni	2.00	1.00	4.00	7.00	<1	<1	2.00	1.00	1.00	4.00	2.00	11.00
Co	1.00	2.00	2.00	2.00	1.00	1.00	1.00	2.00	2.00	1.00	1.00	29.00
Sc	1.90	1.90	2.70	1.60	3.70	2.80	2.10	2.70	2.90	0.80	3.00	12.90
V	22.00	21.00	19.00	30.00	17.00	18.00	18.00	19.00	31.00	30.00	16.00	235.00
Cu	2.00	2.00	3.00	1.00	1.00	2.00	2.00	1.00	2.00	1.00	10.00	77.00
Pb	28.00	31.00	27.00	24.00	33.00	23.00	23.00	24.00	22.00	15.00	9.00	11.00
Zn	104.00	57.00	56.00	20.00	55.00	74.00	63.00	99.00	74.00	16.00	33.00	142.00
Tl	0.42	0.48	0.29	0.05	0.44	0.46	0.30	0.15	<0.02	<0.02	0.05	0.04
Bi	0.05	0.16	0.08	0.02	0.07	0.07	0.05	0.04	0.08	0.01	0.05	0.01
Cd	<0.5	<0.5	<0.5	<0.5	<0.5	<0.5	<0.5	<0.5	<0.5	<0.5	<0.5	0.70
Sn	8.00	7.00	7.00	9.00	7.00	8.00	8.00	8.00	10.00	12.00	8.00	2.00
W	<1	<1	2.00	1.00	2.00	4.00	4.00	2.00	2.00	3.00	2.00	4.00
Li	10.00	<10	10.00	<10	10.00	<10	<10	<10	<10	<10	<10	10.00
Mo	2.00	1.00	2.00	<1	2.00	4.00	3.00	1.00	<1	<1	1.00	<1
Hg	0.01	<0.005	0.01	<0.005	<0.005	<0.005	<0.005	<0.005	<0.005	<0.005	<0.005	<0.005
As	0.30	0.20	<0.1	0.10	0.20	0.40	0.30	0.10	0.20	<0.1	0.80	0.30
Se	<0.2	<0.2	<0.2	0.20	0.20	0.20	0.30	<0.2	0.30	0.20	0.30	0.40
Sb	<0.05	<0.05	<0.05	<0.05	<0.05	<0.05	<0.05	<0.05	<0.05	<0.05	0.07	<0.05
In	0.06	0.05	0.07	0.05	0.09	0.07	0.05	0.08	0.07	0.01	0.07	0.05

	Termales Gneiss												Unilla Amphibolite
Sample	Group 1						Group 2						CAL-0037R
	CAL-0035RA	CAL-0036R	OPP-0004R	OPP-0013RB	OPP-0037R	OPP-0042RA	OPP-0046R	OPP-0200R	CMR-0041R	OPP-0013RA	OPP-0047R		
IGM	5075334	5075336	5075606	5075618	5075643	5075648	5075653	5075696	5075415	5075617	5075654		5075337
Te	<0.01	0.01	<0.01	<0.01	<0.01	0.01	0.01	0.01	<0.01	<0.01	<0.01		<0.01
La	123.50	41.00	96.10	156.50	10.60	22.50	62.50	103.00	123.00	171.50	128.00		37.80
Ce	229.00	89.20	183.00	209.00	101.00	41.10	113.00	210.00	229.00	59.30	232.00		81.40
Pr	28.30	9.04	21.20	33.50	3.50	4.87	14.05	23.90	29.30	35.80	29.30		10.45
Nd	102.50	33.20	77.60	122.50	12.80	19.60	52.90	86.40	115.00	144.00	110.00		47.80
Sm	19.50	6.72	13.90	22.60	3.58	4.40	10.55	16.70	24.20	30.40	21.10		10.95
Eu	2.30	0.93	1.75	3.13	0.55	0.64	1.39	1.89	2.95	4.48	2.40		3.17
Gd	18.30	6.97	11.55	21.90	4.62	5.82	11.00	14.05	22.80	30.00	19.30		12.05
Tb	2.89	1.20	1.74	3.14	0.93	1.21	1.97	2.20	3.65	4.55	3.08		1.81
Dy	17.20	8.71	11.00	18.40	7.69	8.72	12.85	14.65	22.30	25.30	18.60		10.85
Ho	3.42	1.84	2.21	3.20	1.86	2.02	2.86	2.93	4.71	4.34	3.79		2.18
Er	10.20	5.79	6.88	8.43	6.25	6.88	9.54	8.82	16.35	12.25	11.20		6.51
Tm	1.44	0.93	1.07	1.10	1.06	1.05	1.48	1.35	2.43	1.67	1.63		0.88
Yb	9.61	5.84	7.39	6.50	7.22	7.25	9.25	8.92	16.35	9.13	10.45		5.71
Lu	1.40	0.95	1.17	1.02	1.10	1.08	1.37	1.44	2.52	1.28	1.47		0.80

**ANNEX 2. MODAL COMPOSITION OF THE GUAVIARE COMPLEX ROCKS**

Sample	IGM	Qz	Pl	Fsp	Bt	Ms	Hbl	Hst	Chl	Opq	Zrn	Ttn	Ep	Grt	Others	Petrographic classification	Subgroup	
CMR-0027R-2	5075396	17.70	30.70	7.30	37.00					2.30	0.30	3.30			1.30	Quartz-biotite-feldspar gneiss	Gneiss	
OPP-0013R-B	5075618	26.70	4.00	59.70	4.70	0.01				0.01	5.00	0.01			0.01	Biotite bearing quartz-feldspar gneiss	Gneiss	
OPP-0013R-C	5075619	22.30	28.00	42.70	4.00	0.01				0.70	2.00	0.30			0.01	Biotite bearing quartz-feldspar gneiss	Gneiss	
OPP-0029R	5075635	27.00	4.30	59.40	0.01					6.00	2.00	1.00				Chlorite-quartz-feldspar gneiss	Gneiss	
OPP-0037R	5075643	28.70	5.70	45.30	16.70					2.70	1.00				0.02	Biotite-quartz-feldspar gneiss	Gneiss	
CAL-0035R-A	5075334	32.70	33.30	14.00	8.70					2.00	2.70	0.30	5.30		1.02	Epidote-biotite-quartz-feldspar gneiss	Porphyroclastic gneiss	
CAL-0036R	5075336	28.30	36.00	17.20	11.50	1.30				0.80	1.30	0.01	3.30		0.32	Muscovite-epidote bearing biotite-quartz-feldspar gneiss	Porphyroclastic gneiss	
CMR-0036R	5075410	32.00	16.70	28.30	17.00	0.70				1.30	0.01	0.70	3.30		0.02	Epidote bearing biotite-quartz-feldspar gneiss	Porphyroclastic gneiss	
CMR-0041R	5075415	13.70	53.70	0.30				17.3		3.00	1.70	1.70	7.30		1.30	Epidote-amphibole-quartz-feldspar gneiss	Porphyroclastic gneiss	
OPP-0004R	5075606	27.00	7.00	55.70	9.00	0.01				1.30	0.01				0.03	Biotite-quartz-feldspar gneiss	Porphyroclastic gneiss	
OPP-0041R	5075647	27.70	1.00	57.00	12.70				0.01	1.30	0.01				0.31	Biotite-quartz-feldspar gneiss	Porphyroclastic gneiss	
OPP-0042R-A	5075648	21.00	5.30	60.70	9.00		1.30			1.30	0.01	0.30			1.01	Zoisite-hornblende bearing biotite-quartz-feldspar gneiss	Porphyroclastic gneiss	
OPP-0043R	5075650	27.00	3.70	66.70	0.70					1.70	0.01	0.30			0.02	Biotite bearing quartz-feldspar gneiss	Porphyroclastic gneiss	
OPP-0044R	5075651	29.70	2.70	54.30	10.70	1.30				0.70	0.30	0.30			0.02	Muscovite bearing biotite-quartz-feldspar gneiss	Porphyroclastic gneiss	
OPP-0046R	5075653	27.70	29.70	24.00	6.30			7.00		0.01	1.00	0.01	0.70	3.70		0.01	Epidote bearing biotite-hornblende-quartz-feldspar gneiss	Porphyroclastic gneiss
OPP-0047R	5075654	30.00	42.00	11.00	1.00			11.70		0.01	2.70	0.01	1.70			0.01	Biotite bearing hornblende-quartz-feldspar gneiss	Porphyroclastic gneiss
OPP-0200R	5075696	19.00	21.70	48.50	5.70	1.30				1.00	1.70	0.01	0.70		0.71	Chlorite-muscovite bearing biotite-quartz-feldspar gneiss	Porphyroclastic gneiss	
OPP-0013R-A	5075617	29.00	70.70	0.01						0.30	0.01				0.01	Quartz-feldspar granofels	Granofels	
CAL-0038R	5075338	51.20	23.10	8.30	0.01	14.90				1.70	0.60				0.23	Feldspar-quartz blastomylonite	Blastomylonite	
OPP-0045R	5075652	41.50	29.40	4.30	9.00	6.70			1.30	1.30	0.40	0.01	3.70	1.70	0.72	Garnet bearing biotite-feldspar-quartz blastomylonite	Blastomylonite	
CAL-0037R	5075337	5.00	24.00	0.01		60.70		2.30	5.00		1.30	1.00			0.73	Amphibolite	Amphibolite	
ENA-0003R-A	5075465	71.00	20.30			5.40				2.30	0.70	0.30			0.01	Muscovite-feldspar-quartz granofels	Granoblastic quartzite	
ENA-0003R-C	5075467	70.30	20.30			7.70				1.70	0.01				0.01	Muscovite-feldspar-quartz granofels	Granoblastic quartzite	
ENA-0004R	5075468	75.30	16.30	1.30		6.00				0.01	0.01	0.01			1.00	Muscovite-feldspar quartzite	Granoblastic quartzite	
ENA-0008R	5075472	77.00	14.30	3.70		1.30				3.70	0.01				0.02	Muscovite bearing feldspar quartzite	Granoblastic quartzite	
ENA-0021R	5075485	68.70	13.00			5.00				0.01	0.60				12.7	Muscovite-feldspar-quartz granofels	Granoblastic quartzite	
JDB-0026R-B	5075563	77.00				22.30				0.01	0.01	0.01			0.02	Muscovite quartzite	Granoblastic quartzite	
PAG-0009R	5075708	55.60	24.90	2.40		9.40				1.00		0.01			6.7	Muscovite-feldspar-quartz granofels	Granoblastic quartzite	
PAG-0017R	5075717	75.30	10.30	3.30		11.00				0.01	0.01				0.01	Muscovite-feldspar quartzite	Granoblastic quartzite	
PAG-0019R	5075719	68.40	10.60	4.40		15.60				1.00	0.01				0.01	Muscovite-feldspar-quartz granofels	Granoblastic quartzite	
PAG-0023R	5075723	60.30	25.70	5.30		7.00				1.70	0.01	0.01			0.01	Muscovite-feldspar-quartz granofels	Granoblastic quartzite	
PAG-0025R	5075725	68.00	17.00	2.30		10.70				0.01	0.01	0.01			2.01	Muscovite-feldspar-quartz granofels	Granoblastic quartzite	
JDB-0026R-A	5075562	76.70				23.30				0.01	0.01				0.01	Muscovite quartzite	Schist quartzite	
OPP-0030R	5075636	77.70	6.00	2.00		14.30				0.01					0.01	Feldspar-muscovite quartzite	Schist quartzite	
OPP-0034R	5075640	84.70				11.70				0.01			3.70			Muscovite quartzite	Schist quartzite	
OPP-0035R	5075641	82.00				14.00			4.00	0.01						Muscovite quartzite	Schist quartzite	
OPP-0036R	5075642	75.00				23.70			0.01	0.01	0.01			1.32	Muscovite quartzite	Schist quartzite		
OPP-0038R	5075644	88.30				10.30			0.01	0.01				1.31	Muscovite quartzite	Schist quartzite		
OPP-0039R	5075645	61.10	8.30			23.90				0.70			6.00			Feldspar-muscovite-quartz schist	Schist quartzite	
OPP-0040R	5075646	76.00	0.01			14.30							9.71			Muscovite-quartz schist	Schist quartzite	
OPP-0052R	5075659	81.90				2.70				0.01			15.4			Muscovite-quartz schist	Schist quartzite	
PAG-0020R	5075720	75.30	10.30	2.00		10.30				2.00	0.01					Muscovite-feldspar quartzite	Schist quartzite	

Qz: quartz, Pl: plagioclase, Fsp: feldspar, Mc: microcline, Bt: biotite, Ms: muscovite, Hbl: hornblende, Hst: hastingsite, chl: chlorite, Opq: opaque, Zrn: zircon, Ttn: titanite, Ep: epidote, Grt: garnet. Abbreviations according to Whitney and Evans (2010).

**ANNEX 3. ANALYTICAL DATA FOR U/PB AGE OF THE GUAJARÉ COMPLEX**

Analysis	OPP-0013RC (Feldspar-quartz gneiss)														Observations		
	Isotope ratios							Apparent ages (Ma)									
	U (ppm)	U/Th	206Pb <sup>87</sup> / 207Pb <sup>86</sup>	±	207Pb <sup>87</sup> / 235U <sup>86</sup>	±	206Pb <sup>87</sup> / 238U	±	error	206Pb <sup>87</sup> / 238U <sup>86</sup>	±	207Pb <sup>87</sup> / 235U	±	206Pb <sup>87</sup> / 207Pb <sup>86</sup>	±	Conc (%)	
OPP_0013RC_60	182	0.8	16.6389	2.7	0.8465	3.5	0.1022	2.3	0.65	627.3	13.5	622.7	16.2	607.2	57.6	103.3	Partial Pb-loss? Recrystallization?
OPP_0013RC_07	237	3.4	11.6414	3.1	1.3851	9.9	0.1170	9.4	0.95	713.3	63.5	882.6	58.5	1335.9	60.8	53.4	Partial Pb-loss? Recrystallization?
OPP_0013RC_15	311	3.8	12.3305	2.0	1.7425	5.1	0.1559	4.7	0.92	934.0	41.3	1024.4	33.2	1223.9	38.8	76.3	Partial Pb-loss? Recrystallization?
OPP_0013RC_45	225	5.5	12.4688	2.7	2.1222	5.9	0.1920	5.2	0.88	1132.2	54.1	1156.0	40.6	1201.9	54.1	94.2	Partial Pb-loss? Recrystallization?
OPP_0013RC_66	43	1.9	11.8483	3.0	2.4264	4.1	0.2086	2.8	0.68	1221.4	30.9	1250.5	29.2	1301.8	57.6	93.8	Igneous protolith
OPP_0013RC_38	204	1.4	12.0627	1.9	2.4221	2.9	0.2120	2.2	0.75	1239.5	24.5	1249.2	20.9	1266.9	37.7	97.8	Igneous protolith
OPP_0013RC_35	365	1.2	11.7371	2.0	2.4905	2.6	0.2121	1.6	0.63	1240.0	18.1	1269.3	18.5	1320.1	38.7	93.9	Igneous protolith
OPP_0013RC_50	186	1.8	11.8203	2.1	2.5068	3.0	0.2150	2.1	0.70	1255.4	23.9	1274.0	21.7	1306.4	41.3	96.1	Igneous protolith
OPP_0013RC_18	112	1.7	11.8624	2.1	2.5002	3.0	0.2152	2.1	0.71	1256.5	24.4	1272.1	21.9	1299.5	41.5	96.7	Igneous protolith
OPP_0013RC_30	9	1.6	11.6279	6.5	2.5684	7.4	0.2167	3.6	0.48	1264.4	41.3	1291.7	54.4	1338.2	126.0	94.5	Igneous protolith
OPP_0013RC_25	156	1.9	11.9190	3.1	2.5103	3.8	0.2171	2.2	0.57	1266.5	24.9	1275.0	27.5	1290.2	60.3	98.2	Igneous protolith
OPP_0013RC_48	111	1.0	12.1655	2.6	2.4753	3.4	0.2185	2.2	0.66	1273.9	25.9	1264.8	24.6	1250.3	50.0	101.9	Igneous protolith
OPP_0013RC_49	83	1.7	11.7096	3.6	2.5717	4.4	0.2185	2.5	0.56	1273.9	28.6	1292.6	32.1	1324.6	70.3	96.2	Igneous protolith
OPP_0013RC_65	127	1.5	11.6144	2.1	2.5987	2.9	0.2190	2.1	0.70	1276.6	23.8	1300.3	21.5	1340.4	40.4	95.2	Igneous protolith
OPP_0013RC_70	139	1.9	11.8064	2.1	2.5599	3.2	0.2193	2.3	0.74	1278.2	27.0	1289.3	23.0	1308.7	41.2	97.7	Igneous protolith
OPP_0013RC_51	271	1.4	12.0337	1.6	2.5139	3.0	0.2195	2.6	0.86	1279.2	30.1	1276.0	22.0	1271.6	30.5	100.6	Igneous protolith
OPP_0013RC_46	60	1.5	11.4155	2.6	2.6536	3.5	0.2198	2.4	0.67	1280.8	27.5	1315.6	26.1	1373.7	50.5	93.2	Igneous protolith
OPP_0013RC_64	197	1.9	11.7233	1.8	2.5839	2.5	0.2198	1.8	0.72	1280.8	21.1	1296.1	18.5	1322.3	34.1	96.9	Igneous protolith
OPP_0013RC_55	56	1.8	11.9474	3.1	2.5389	3.8	0.2201	2.1	0.57	1282.4	24.8	1283.3	27.5	1285.6	60.5	99.8	Igneous protolith
OPP_0013RC_54	142	1.9	11.8343	2.4	2.5702	3.2	0.2207	2.2	0.68	1285.6	25.9	1292.2	23.7	1304.1	46.0	98.6	Igneous protolith
OPP_0013RC_17	159	1.8	11.8483	2.3	2.5706	2.8	0.2210	1.6	0.58	1287.2	18.5	1292.3	20.1	1301.8	43.7	98.9	Igneous protolith
OPP_0013RC_56	438	1.5	11.9617	2.2	2.5509	3.1	0.2214	2.2	0.72	1289.3	25.9	1286.7	22.5	1283.2	41.9	100.5	Igneous protolith
OPP_0013RC_42	109	1.7	11.8765	3.7	2.5715	4.6	0.2216	2.8	0.61	1290.3	32.7	1292.6	33.8	1297.2	71.6	99.5	Igneous protolith
OPP_0013RC_26	42	1.1	11.7786	4.0	2.5941	4.6	0.2217	2.3	0.50	1290.9	26.9	1299.0	33.9	1313.2	77.7	98.3	Igneous protolith
OPP_0013RC_59	108	2.1	12.0919	2.7	2.5268	3.9	0.2217	2.8	0.72	1290.9	32.7	1279.8	28.1	1262.1	52.0	102.3	Igneous protolith
OPP_0013RC_43	126	1.7	11.9048	2.4	2.5723	3.4	0.2222	2.4	0.71	1293.5	28.5	1292.8	24.9	1292.5	46.3	100.1	Igneous protolith
OPP_0013RC_05	109	2.1	11.6959	2.8	2.6242	3.4	0.2227	2.0	0.58	1296.1	23.2	1307.4	25.2	1326.9	54.4	97.7	Igneous protolith
OPP_0013RC_04	122	1.9	11.8203	1.8	2.6024	2.7	0.2232	2.0	0.74	1298.8	23.2	1301.3	19.5	1306.4	34.4	99.4	Igneous protolith
OPP_0013RC_09	116	1.7	11.5075	2.2	2.6755	3.0	0.2234	2.1	0.69	1299.8	24.8	1321.7	22.4	1358.3	42.2	95.7	Igneous protolith
OPP_0013RC_10	244	1.7	11.6414	2.0	2.6447	2.4	0.2234	1.4	0.59	1299.8	16.9	1313.2	18.0	1335.9	38.3	97.3	Igneous protolith
OPP_0013RC_53	153	1.8	11.8343	1.9	2.6040	2.7	0.2236	2.0	0.72	1300.9	23.2	1301.8	20.0	1304.1	36.8	99.8	Igneous protolith
OPP_0013RC_72	83	2.0	11.7647	2.0	2.6217	2.8	0.2238	2.0	0.70	1301.9	23.2	1306.7	20.6	1315.5	38.8	99.0	Igneous protolith
OPP_0013RC_08	194	1.8	11.6279	2.0	2.6537	2.6	0.2239	1.7	0.64	1302.4	19.5	1315.7	19.0	1338.2	38.2	97.3	Igneous protolith
OPP_0013RC_58	83	1.5	11.9474	2.9	2.5828	3.6	0.2239	2.2	0.61	1302.4	26.3	1295.8	26.6	1285.6	55.8	101.3	Igneous protolith
OPP_0013RC_63	184	1.8	11.6959	2.1	2.6383	2.6	0.2239	1.6	0.61	1302.4	19.0	1311.4	19.5	1326.9	40.8	98.2	Igneous protolith
OPP_0013RC_67	119	2.0	11.6144	1.9	2.6616	3.0	0.2243	2.4	0.79	1304.6	27.9	1317.9	22.2	1340.4	35.9	97.3	Igneous protolith
OPP_0013RC_27	37	1.2	11.7233	4.2	2.6427	4.8	0.2248	2.2	0.47	1307.2	26.3	1312.6	35.2	1322.3	81.8	98.9	Igneous protolith
OPP_0013RC_21	183	1.3	11.6414	2.0	2.6637	2.6	0.2250	1.7	0.66	1308.2	20.5	1318.4	19.4	1335.9	38.3	97.9	Igneous protolith
OPP_0013RC_13	544	1.4	11.7371	1.5	2.6443	2.3	0.2252	1.8	0.76	1309.3	21.0	1313.1	17.3	1320.1	29.6	99.2	Igneous protolith
OPP_0013RC_03	135	1.6	11.6822	2.2	2.6579	3.0	0.2253	2.0	0.66	1309.8	23.1	1316.8	21.8	1329.1	43.0	98.5	Igneous protolith
OPP_0013RC_12	186	1.6	11.6822	1.5	2.6591	2.3	0.2254	1.8	0.76	1310.3	21.0	1317.2	17.2	1329.1	29.4	98.6	Igneous protolith
OPP_0013RC_19	165	1.8	11.8483	2.3	2.6253	3.1	0.2257	2.2	0.69	1311.9	25.8	1307.8	23.0	1301.8	43.7	100.8	Igneous protolith
OPP_0013RC_16	78	1.6	11.9760	2.5	2.5996	3.1	0.2259	1.7	0.57	1313.0	20.5	1300.5	22.4	1280.9	49.0	102.5	Igneous protolith
OPP_0013RC_44	111	1.9	11.9048	2.1	2.6152	2.8	0.2259	1.7	0.63	1313.0	20.5	1304.9	20.2	1292.5	41.7	101.6	Igneous protolith
OPP_0013RC_11	136	1.7	11.8906	2.1	2.6195	2.7	0.2260	1.7	0.62	1313.5	20.0	1306.1	20.0	1294.8	41.6	101.4	Igneous protolith
OPP_0013RC_71	88	1.8	11.8343	2.1	2.6319	2.9	0.2260	2.0	0.69	1313.5	24.2	1309.6	21.7	1304.1	41.4	100.7	Igneous protolith
OPP_0013RC_73	213	1.6	11.6009	1.4	2.6849	2.4	0.2260	1.9	0.81	1313.5	23.1	1324.3	17.7	1342.7	26.9	97.8	Igneous protolith
OPP_0013RC_62	323	1.7	11.8906	1.7	2.6218	2.4	0.2262	1.8	0.73	1314.6	21.0	1306.8	17.9	1294.8	32.4	101.5	Igneous protolith
OPP_0013RC_22	125	0.9	11.9474	1.9	2.6105	3.0	0.2263	2.3	0.77	1315.1	27.3	1303.6	21.9	1285.6	37.2	102.3	Igneous protolith

OPP-0013RC (Feldspar-quartz gneiss)																	
Analysis	Isotope ratios										Apparent ages (Ma)						Observations
	U	U/Th	206Pb <sup>87</sup> /	±	207Pb <sup>87</sup> /	±	206Pb <sup>87</sup> /	±	error	206Pb <sup>87</sup> /	±	207Pb <sup>87</sup> /	±	206Pb <sup>87</sup> /	±	Conc	
	(ppm)		207Pb <sup>87</sup>	(%)	235U <sup>87</sup>	(%)	238U	(%)	corr.	238U <sup>87</sup>	(Ma)	235U	(Ma)	207Pb <sup>87</sup>	(Ma)	(%)	
OPP_0013RC_75	109	1.9	11.7786	2.1	2.6479	2.8	0.2263	1.8	0.65	1315.1	21.6	1314.1	20.6	1313.2	41.1	100.1	Igneous protolith
OPP_0013RC_69	134	1.8	11.7233	1.9	2.6674	2.5	0.2269	1.7	0.67	1318.2	20.0	1319.5	18.6	1322.3	36.3	99.7	Igneous protolith
OPP_0013RC_40	128	1.7	11.7786	1.9	2.6584	2.6	0.2272	1.8	0.70	1319.8	22.1	1317.0	19.5	1313.2	36.6	100.5	Igneous protolith
OPP_0013RC_34	122	1.7	11.7509	2.5	2.6682	3.1	0.2275	1.8	0.60	1321.4	22.1	1319.7	22.8	1317.8	47.8	100.3	Igneous protolith
OPP_0013RC_74	248	1.9	11.8765	1.5	2.6446	2.5	0.2279	2.0	0.79	1323.5	23.6	1313.1	18.5	1297.2	30.0	102.0	Igneous protolith
OPP_0013RC_61	263	1.8	11.6822	1.8	2.6898	2.7	0.2280	2.0	0.75	1324.0	24.1	1325.6	19.8	1329.1	33.9	99.6	Igneous protolith
OPP_0013RC_06	128	2.1	11.9048	2.0	2.6430	2.6	0.2283	1.7	0.64	1325.6	19.9	1312.7	19.3	1292.5	39.4	102.6	Igneous protolith
OPP_0013RC_02	105	1.6	11.9048	1.9	2.6453	2.6	0.2285	1.8	0.69	1326.6	21.5	1313.3	19.3	1292.5	37.0	102.6	Igneous protolith
OPP_0013RC_37	171	1.6	11.7647	1.8	2.6779	2.3	0.2286	1.5	0.64	1327.2	17.8	1322.4	17.1	1315.5	34.2	100.9	Igneous protolith
OPP_0013RC_29	13	1.4	11.9760	5.4	2.6330	5.8	0.2288	2.1	0.37	1328.2	25.7	1309.9	42.7	1280.9	105.1	103.7	Igneous protolith
OPP_0013RC_20	165	1.8	11.5340	2.4	2.7351	3.2	0.2289	2.1	0.65	1328.7	25.2	1338.0	23.8	1353.8	46.7	98.1	Igneous protolith
OPP_0013RC_47	82	1.8	11.6009	2.1	2.7193	3.0	0.2289	2.1	0.71	1328.7	25.2	1333.7	22.0	1342.7	40.3	99.0	Igneous protolith
OPP_0013RC_36	150	1.8	11.6009	2.4	2.7205	3.2	0.2290	2.0	0.64	1329.3	24.1	1334.1	23.4	1342.7	47.1	99.0	Igneous protolith
OPP_0013RC_23	75	1.6	12.1507	4.7	2.6076	6.0	0.2299	3.7	0.61	1334.0	44.0	1302.8	43.9	1252.6	92.8	106.5	Igneous protolith
OPP_0013RC_14	647	1.6	11.6959	1.6	2.7102	2.3	0.2300	1.7	0.71	1334.5	19.9	1331.3	17.3	1326.9	31.7	100.6	Igneous protolith
OPP_0013RC_68	117	2.1	11.6279	2.8	2.7320	3.5	0.2305	2.2	0.61	1337.1	26.2	1337.2	26.3	1338.2	54.0	99.9	Igneous protolith
OPP_0013RC_28	67	1.9	11.9332	3.5	2.6667	4.1	0.2309	2.3	0.55	1339.2	27.2	1319.3	30.5	1287.9	67.4	104.0	Igneous protolith
OPP_0013RC_39	117	2.0	11.8906	2.3	2.6786	3.1	0.2311	2.1	0.68	1340.3	25.7	1322.6	22.9	1294.8	43.9	103.5	Igneous protolith
OPP_0013RC_57	221	1.7	11.8064	2.0	2.6977	2.9	0.2311	2.1	0.73	1340.3	25.7	1327.8	21.6	1308.7	39.0	102.4	Igneous protolith
OPP_0013RC_01	267	2.1	11.8906	1.5	2.6844	2.4	0.2316	1.9	0.78	1342.9	23.0	1324.2	18.1	1294.8	30.1	103.7	Igneous protolith
OPP_0013RC_24	271	1.6	11.7925	1.8	2.7079	2.5	0.2317	1.8	0.71	1343.4	21.5	1330.6	18.6	1311.0	34.3	102.5	Igneous protolith
OPP_0013RC_31	314	1.2	22.0264	5.3	0.0910	5.8	0.0146	2.3	0.39	93.1	2.1	88.5	4.9	-34.1	128.3	NA	Contamination?
OPP_0013RC_32	128	2.3	21.2314	8.5	0.0968	9.0	0.0149	3.0	0.33	95.4	2.9	93.8	8.1	54.3	202.9	NA	Contamination?
OPP_0013RC_33	230	1.3	15.0602	8.1	0.1385	8.4	0.0151	2.2	0.27	96.8	2.2	131.7	10.4	819.0	170.1	NA	Contamination?

CAL-0037R (Amphibolite)																	
Analysis	Isotope ratios										Apparent ages (Ma)						Observations
	U	U/Th	206Pb <sup>87</sup> /	±	207Pb <sup>87</sup> /	±	206Pb <sup>87</sup> /	±	error	206Pb <sup>87</sup> /	±	207Pb <sup>87</sup> /	±	206Pb <sup>87</sup> /	±	Conc	
	(ppm)		207Pb <sup>87</sup>	(%)	235U <sup>87</sup>	(%)	238U	(%)	corr.	238U <sup>87</sup>	(Ma)	235U	(Ma)	207Pb <sup>87</sup>	(Ma)	(%)	
CAL_0037R_03	228	1.1	15.6740	2.8	0.8151	3.8	0.0927	2.5	0.66	571.5	13.6	605.3	17.1	735.0	59.7	77.8	Partial Pb-loss? Recrystallization?
CAL_0037R_20	474	3.7	13.3511	2.3	1.7249	3.8	0.1671	3.0	0.80	996.1	27.6	1017.9	24.1	1065.8	45.6	93.5	Partial Pb-loss? Recrystallization?
CAL_0037R_24	281	1.0	11.7509	2.5	2.0267	3.7	0.1728	2.7	0.74	1027.5	25.8	1124.5	25.0	1317.8	47.8	78.0	Partial Pb-loss? Recrystallization?
CAL_0037R_13	766	1.6	11.6686	1.5	2.0799	3.8	0.1761	3.5	0.92	1045.6	33.4	1142.2	25.9	1331.4	29.4	78.5	Partial Pb-loss? Recrystallization?
CAL_0037R_18	953	1.8	11.7786	1.3	2.1869	2.3	0.1869	1.9	0.83	1104.6	19.6	1176.9	16.2	1313.2	25.1	84.1	Partial Pb-loss? Recrystallization?
CAL_0037R_07	219	3.2	12.2549	2.0	2.2728	2.6	0.2021	1.6	0.64	1186.6	17.7	1203.9	18.0	1236.0	38.4	96.0	Partial Pb-loss? Recrystallization?
CAL_0037R_40	352	2.3	11.9760	1.6	2.3499	2.2	0.2042	1.6	0.71	1197.8	17.1	1227.5	15.7	1280.9	30.3	93.5	Partial Pb-loss? Recrystallization?
CAL_0037R_09	161	1.7	11.7509	2.2	2.5321	2.6	0.2159	1.3	0.52	1260.2	15.4	1281.3	19.0	1317.8	43.3	95.6	Partial Pb-loss? Recrystallization?
CAL_0037R_34	581	1.7	11.6550	1.4	2.6026	2.1	0.2201	1.5	0.74	1282.4	18.0	1301.4	15.3	1333.7	27.1	96.2	Igneous protolith
CAL_0037R_23	180	1.8	11.8343	2.4	2.5655	2.9	0.2203	1.6	0.56	1283.5	18.5	1290.9	20.8	1304.1	46.0	98.4	Igneous protolith
CAL_0037R_08	147	1.6	11.7647	2.2	2.5913	2.7	0.2212	1.4	0.54	1288.2	16.9	1298.2	19.5	1315.5	43.3	97.9	Igneous protolith
CAL_0037R_10	101	2.3	11.7233	2.3	2.6028	2.9	0.2214	1.8	0.60	1289.3	20.6	1301.4	21.5	1322.3	45.4	97.5	Igneous protolith
CAL_0037R_02	144	1.7	11.8765	1.7	2.5727	2.3	0.2217	1.6	0.70	1290.9	19.0	1292.9	17.0	1297.2	32.3	99.5	Igneous protolith
CAL_0037R_14	811	1.1	11.8765	1.7	2.5727	2.5	0.2217	1.8	0.74	1290.9	21.6	1292.9	18.2	1297.2	32.3	99.5	Igneous protolith
CAL_0037R_35	188	1.7	11.8483	2.0	2.5881	2.7	0.2225	1.8	0.66	1295.1	20.6	1297.3	19.6	1301.8	39.1	99.5	Igneous protolith
CAL_0037R_15	206	1.7	11.7647	1.4	2.6229	2.1	0.2239	1.6	0.75	1302.4	19.0	1307.1	15.7	1315.5	27.4	99.0	Igneous protolith
CAL_0037R_11	378	1.9	11.7509	1.5	2.6342	2.3	0.2246	1.7	0.75	1306.1	20.5	1310.2	17.0	1317.8	29.6	99.1	Igneous protolith
CAL_0037R_21	514	1.3	11.6959	1.3	2.6477	2.1	0.2247	1.7	0.80	1306.7	20.0	1314.0	15.7	1326.9	24.9	98.5	Igneous protolith
CAL_0037R_37	197	1.5	11.7233	2.0	2.6451	2.6	0.2250	1.7	0.66	1308.2	20.5	1313.3	19.5	1322.3	38.6	98.9	Igneous protolith
CAL_0037R_22	539	1.4	11.8483	1.4	2.6207	2.2	0.2253	1.7	0.77	1309.8	20.5	1306.4	16.5	1301.8	27.6	100.6	Igneous protolith
CAL_0037R_01	146	1.6	12.0773	1.9	2.5767	2.6	0.2258	1.8	0.68	1312.4	21.0	1294.0	19.2	1264.5	37.7	103.8	Igneous protolith

CAL-0037R (Amphibolite)																	
Analysis	Isotope ratios										Apparent ages (Ma)						Observations
	U	U/Th	206Pb <sup>87</sup> /	±	207Pb <sup>87</sup> /	±	206Pb <sup>87</sup> /	±	error	206Pb <sup>87</sup> /	±	207Pb <sup>87</sup> /	±	206Pb <sup>87</sup> /	±	Conc	
	(ppm)		207Pb <sup>87</sup>	(%)	235U <sup>87</sup>	(%)	238U	(%)	corr.	238U <sup>87</sup>	(Ma)	235U	(Ma)	207Pb <sup>87</sup>	(Ma)	(%)	
CAL_0037R_17	901	1.3	11.7233	1.4	2.6557	2.2	0.2259	1.7	0.77	1313.0	20.0	1316.2	16.2	1322.3	27.3	99.3	Igneous protolith
CAL_0037R_12	931	2.5	11.6414	1.7	2.6909	2.3	0.2273	1.5	0.64	1320.3	17.3	1326.0	16.8	1335.9	33.8	98.8	Igneous protolith
CAL_0037R_27	531	1.6	11.8064	1.4	2.6615	2.5	0.2280	2.1	0.82	1324.0	24.7	1317.8	18.5	1308.7	27.5	101.2	Igneous protolith
CAL_0037R_26	858	1.9	11.8343	1.8	2.6703	2.7	0.2293	2.0	0.76	1330.8	24.6	1320.3	20.0	1304.1	34.5	102.1	Igneous protolith
CAL_0037R_32	82	1.5	11.8906	2.6	2.6600	3.4	0.2295	2.2	0.65	1331.9	26.7	1317.4	25.3	1294.8	50.9	102.9	Igneous protolith
CAL_0037R_25	442	1.3	11.7925	1.8	2.6868	2.7	0.2299	2.0	0.75	1334.0	24.1	1324.8	19.8	1311.0	34.3	101.8	Igneous protolith
CAL_0037R_28	411	2.9	9.4787	1.3	4.7269	2.1	0.3251	1.6	0.78	1814.6	25.8	1772.0	17.6	1723.0	24.4	105.3	Inherit
CAL_0037R_29	141	0.8	9.0416	2.2	4.5576	3.2	0.2990	2.4	0.74	1686.3	35.2	1741.5	26.8	1809.3	39.4	93.2	Inherit
CAL_0037R_05	94	0.9	19.2308	9.0	0.1048	9.3	0.0146	2.3	0.25	93.6	2.2	101.2	9.0	285.4	207.0	NA	Contamination?
CAL_0037R_33	650	1.5	20.3252	4.1	0.0996	4.6	0.0147	2.1	0.46	94.0	2.0	96.4	4.2	157.4	95.2	NA	Contamination?
CAL_0037R_06	71	1.0	20.5761	11.7	0.1019	12.1	0.0152	3.2	0.26	97.3	3.0	98.5	11.4	128.6	276.8	NA	Contamination?
CAL_0037R_36	344	1.7	21.8818	5.9	0.0958	6.5	0.0152	2.6	0.41	97.3	2.5	92.9	5.7	-18.2	143.0	NA	Contamination?
OPP-0036R (Quartzite)																	
Analysis	Isotope ratios										Apparent ages (Ma)						Observations
	U	U/Th	206Pb <sup>87</sup> /	±	207Pb <sup>87</sup> /	±	206Pb <sup>87</sup> /	±	error	206Pb <sup>87</sup> /	±	207Pb <sup>87</sup> /	±	206Pb <sup>87</sup> /	±	Conc	
	(ppm)		207Pb <sup>87</sup>	(%)	235U <sup>87</sup>	(%)	238U	(%)	corr.	238U <sup>87</sup>	(Ma)	235U	(Ma)	207Pb <sup>87</sup>	(Ma)	(%)	
OPP_0036R_01	162	0.7	9.8039	1.7	4.1441	2.3	0.2948	1.5	0.68	1665.5	22.4	1663.1	18.5	1660.8	30.9	100.3	D detrital zircon
OPP_0036R_02	227	1.4	9.6432	1.6	4.1932	2.1	0.2934	1.3	0.63	1658.5	19.4	1672.7	17.3	1691.4	30.2	98.1	D detrital zircon
OPP_0036R_03	119	2.3	9.6618	1.8	4.1395	2.7	0.2902	1.9	0.72	1642.5	28.0	1662.1	21.8	1687.8	33.9	97.3	D detrital zircon
OPP_0036R_04	129	1.6	9.4967	1.6	4.4103	2.3	0.3039	1.6	0.70	1710.6	23.7	1714.3	18.7	1719.5	29.7	99.5	D detrital zircon
OPP_0036R_05	483	0.8	10.5820	1.5	3.2234	2.1	0.2475	1.5	0.71	1425.6	19.1	1462.8	16.3	1518.1	27.9	93.9	D detrital zircon
OPP_0036R_06	346	1.6	8.0451	1.4	6.1705	2.3	0.3602	1.7	0.77	1983.1	29.9	2000.3	19.8	2018.8	25.7	98.2	D detrital zircon
OPP_0036R_07	343	1.5	7.9745	1.4	6.1283	2.3	0.3546	1.7	0.77	1956.5	29.5	1994.3	19.7	2034.4	25.4	96.2	D detrital zircon
OPP_0036R_08	314	1.5	9.4073	1.4	4.3877	2.1	0.2995	1.5	0.73	1688.8	22.3	1710.0	17.0	1736.9	25.9	97.2	D detrital zircon
OPP_0036R_09	170	1.3	6.0938	1.6	10.4667	2.4	0.4628	1.7	0.72	2451.9	34.8	2477.0	22.0	2498.3	27.7	98.1	D detrital zircon
OPP_0036R_10	153	1.2	5.9277	1.4	10.9275	2.0	0.4700	1.5	0.74	2483.6	30.7	2517.0	18.8	2544.8	22.8	97.6	D detrital zircon
OPP_0036R_11	125	1.2	9.8814	2.3	3.7964	2.9	0.2722	1.8	0.63	1552.0	25.3	1592.0	23.5	1646.2	42.2	94.3	D detrital zircon
OPP_0036R_12	67	1.6	10.2249	2.7	3.8360	3.5	0.2846	2.2	0.64	1614.5	31.6	1600.3	27.9	1582.6	49.7	102.0	D detrital zircon
OPP_0036R_13	397	1.5	9.0009	1.5	4.9089	2.3	0.3206	1.7	0.75	1792.7	27.3	1803.8	19.6	1817.5	27.8	98.6	D detrital zircon
OPP_0036R_14	194	1.1	10.4167	2.2	3.3500	2.7	0.2532	1.6	0.59	1455.0	21.1	1492.8	21.3	1547.8	41.1	94.0	D detrital zircon
OPP_0036R_15	149	1.3	11.9048	2.0	2.5307	2.6	0.2186	1.6	0.63	1274.5	19.0	1280.9	19.0	1292.5	39.4	98.6	D detrital zircon
OPP_0036R_16	347	1.0	9.3284	1.6	4.4175	2.4	0.2990	1.8	0.76	1686.3	27.3	1715.6	20.1	1752.3	29.0	96.2	D detrital zircon
OPP_0036R_17	220	0.9	10.9409	1.8	3.2222	2.2	0.2558	1.4	0.62	1468.3	18.0	1462.5	17.2	1454.9	33.3	100.9	D detrital zircon
OPP_0036R_18	188	1.7	11.8906	1.9	2.5430	2.5	0.2194	1.5	0.63	1278.7	18.0	1284.4	17.9	1294.8	37.0	98.8	D detrital zircon
OPP_0036R_19	308	1.2	9.3721	1.4	4.4924	1.9	0.3055	1.3	0.67	1718.5	19.3	1729.6	15.8	1743.8	25.8	98.6	D detrital zircon
OPP_0036R_20	281	0.8	10.9051	1.4	3.1405	2.0	0.2485	1.4	0.71	1430.7	18.6	1442.7	15.6	1461.2	26.9	97.9	D detrital zircon
OPP_0036R_21	31	0.5	10.3093	4.1	3.3207	4.8	0.2484	2.4	0.50	1430.2	30.5	1485.9	37.2	1567.2	77.3	91.3	D detrital zircon
OPP_0036R_22	35	0.5	10.7527	3.0	3.1107	3.9	0.2427	2.4	0.63	1400.7	30.6	1435.3	29.7	1487.9	57.0	94.1	D detrital zircon
OPP_0036R_23	301	1.6	9.1241	1.5	4.7686	2.5	0.3157	2.0	0.81	1768.7	31.4	1779.4	21.0	1792.8	26.6	98.7	D detrital zircon
OPP_0036R_24	159	1.4	9.2421	1.6	4.5720	2.7	0.3066	2.2	0.81	1724.0	32.6	1744.2	22.2	1769.3	28.7	97.4	D detrital zircon
OPP_0036R_25	253	1.2	9.3458	1.6	4.5464	2.5	0.3083	1.9	0.77	1732.3	29.6	1739.5	20.9	1748.9	29.1	99.1	D detrital zircon
OPP_0036R_26	102	1.3	10.9890	2.1	2.9849	2.6	0.2380	1.5	0.59	1376.3	18.7	1403.8	19.6	1446.6	39.8	95.1	D detrital zircon
OPP_0036R_27	240	1.4	11.9904	1.6	2.4885	2.1	0.2165	1.5	0.69	1263.4	17.0	1268.7	15.6	1278.6	30.4	98.8	D detrital zircon
OPP_0036R_28	733	1.3	9.7561	1.6	3.8438	2.2	0.2721	1.5	0.70	1551.5	21.3	1602.0	17.7	1669.9	28.9	92.9	D detrital zircon
OPP_0036R_29	152	1.1	9.7087	1.7	4.1280	2.7	0.2908	2.1	0.76	1645.5	30.0	1659.9	22.1	1678.9	32.3	98.0	D detrital zircon
OPP_0036R_30	163	0.8	9.5329	1.9	3.8311	2.8	0.2650	2.1	0.74	1515.4	28.5	1599.3	22.9	1712.5	35.1	88.5	D detrital zircon
OPP_0036R_31	75	1.5	9.5694	2.3	4.0225	2.9	0.2793	1.8	0.61	1587.8	25.2	1638.7	23.7	1705.5	42.3	93.1	D detrital zircon
OPP_0036R_32	50	1.0	9.8135	3.0	3.7609	3.7	0.2678	2.2	0.58	1529.6	29.5	1584.4	30.0	1659.0	56.3	92.2	D detrital zircon
OPP_0036R_33	160	1.4	10.6157	1.6	3.3832	2.0	0.2606	1.3	0.62	1492.9	16.9	1500.5	15.9	1512.1	30.1	98.7	D detrital zircon
OPP_0036R_34	115	1.9	10.6383	1.8	3.3268	2.5	0.2568	1.8	0.70	1473.4	23.6	1487.4	19.9	1508.1	34.2	97.7	D detrital zircon
OPP_0036R_35	141	3.0	10.4822	2.1	3.4263	2.8	0.2606	1.8	0.66	1492.9	24.5	1510.5	21.9	1536.0	39.5	97.2	D detrital zircon

OPP-0036R (Quartzite)																	
Analysis	Isotope ratios										Apparent ages (Ma)						Observations
	U	U/Th	206Pb <sup>87</sup> /	±	207Pb <sup>87</sup> /	±	206Pb <sup>87</sup> /	±	error	206Pb <sup>87</sup> /	±	207Pb <sup>87</sup> /	±	206Pb <sup>87</sup> /	±	Conc	
	(ppm)		207Pb <sup>87</sup>	(%)	235U <sup>87</sup>	(%)	238U	(%)	corr.	238U <sup>87</sup>	(Ma)	235U	(Ma)	207Pb <sup>87</sup>	(Ma)	(%)	
OPP_0036R_36	81	0.9	10.6610	3.0	3.3443	3.5	0.2587	1.9	0.53	1483.2	24.6	1491.5	27.5	1504.1	56.4	98.6	Detrital zircon
OPP_0036R_37	70	1.0	10.2041	2.3	3.3441	3.0	0.2476	1.9	0.63	1426.1	24.3	1491.4	23.6	1586.4	43.9	89.9	Detrital zircon
OPP_0036R_38	268	17.4	5.4377	1.2	12.8092	1.8	0.5054	1.3	0.73	2637.0	27.8	2665.7	16.5	2688.3	19.8	98.1	Detrital zircon
OPP_0036R_39	91	1.2	9.4073	2.2	4.5181	2.9	0.3084	1.9	0.67	1732.8	29.6	1734.3	24.2	1736.9	39.7	99.8	Detrital zircon
OPP_0036R_40	83	2.0	11.7233	2.7	2.6451	3.3	0.2250	1.9	0.57	1308.2	22.1	1313.3	24.2	1322.3	52.2	98.9	Detrital zircon
OPP_0036R_41	291	1.5	9.4877	1.6	4.1399	2.4	0.2850	1.8	0.74	1616.5	25.6	1662.2	19.7	1721.3	29.6	93.9	Detrital zircon
OPP_0036R_42	132	1.5	9.3197	1.8	4.4423	2.3	0.3004	1.5	0.65	1693.3	22.3	1720.3	19.2	1754.0	32.4	96.5	Detrital zircon
OPP_0036R_43	222	1.5	9.7276	1.5	4.0576	2.0	0.2864	1.4	0.69	1623.5	20.0	1645.8	16.5	1675.3	27.0	96.9	Detrital zircon
OPP_0036R_44	86	1.2	10.5042	2.7	3.1777	3.2	0.2422	1.7	0.53	1398.1	21.3	1451.8	24.8	1532.0	51.4	91.3	Detrital zircon
OPP_0036R_45	161	1.5	11.0132	2.1	3.0634	2.8	0.2448	1.8	0.65	1411.6	22.8	1423.6	21.1	1442.4	39.9	97.9	Detrital zircon
OPP_0036R_46	242	7.0	9.4518	1.7	4.5712	2.2	0.3135	1.4	0.64	1757.9	21.6	1744.0	18.4	1728.2	31.2	101.7	Detrital zircon
OPP_0036R_47	60	1.1	11.2233	2.1	3.0453	2.9	0.2480	2.0	0.68	1428.2	25.3	1419.1	22.2	1406.3	40.8	101.6	Detrital zircon
OPP_0036R_48	49	0.7	10.7643	3.1	3.2751	3.7	0.2558	2.1	0.55	1468.3	27.2	1475.2	29.2	1485.8	59.1	98.8	Detrital zircon
OPP_0036R_49	706	2.3	10.5708	1.5	3.3507	2.1	0.2570	1.6	0.72	1474.5	20.5	1492.9	16.8	1520.1	27.9	97.0	Detrital zircon
OPP_0036R_50	159	1.5	11.0742	2.2	3.1312	3.2	0.2516	2.3	0.72	1446.7	29.4	1440.4	24.4	1431.9	42.3	101.0	Detrital zircon
OPP_0036R_51	85	1.0	9.4518	1.5	4.1833	2.3	0.2869	1.7	0.76	1626.0	25.0	1670.8	18.9	1728.2	27.8	94.1	Detrital zircon
OPP_0036R_52	305	1.3	9.4162	1.7	4.4319	2.5	0.3028	1.9	0.74	1705.2	28.2	1718.3	21.0	1735.2	31.1	98.3	Detrital zircon
OPP_0036R_53	180	1.5	9.5694	1.5	4.4949	2.6	0.3121	2.1	0.80	1751.0	31.4	1730.0	21.3	1705.5	28.2	102.7	Detrital zircon
OPP_0036R_54	357	1.8	8.6806	1.3	5.1885	2.2	0.3268	1.8	0.81	1822.9	28.7	1850.7	19.0	1883.0	23.5	96.8	Detrital zircon
OPP_0036R_55	62	1.3	10.2669	3.1	3.5156	3.5	0.2619	1.7	0.48	1499.6	22.5	1530.7	27.7	1574.9	57.7	95.2	Detrital zircon
OPP_0036R_56	25	1.1	12.2399	3.8	2.5188	4.3	0.2237	2.0	0.46	1301.4	23.2	1277.5	31.1	1238.4	74.4	105.1	Detrital zircon
OPP_0036R_57	117	1.2	9.1075	1.8	4.8530	2.4	0.3207	1.5	0.64	1793.1	23.9	1794.1	20.0	1796.1	33.2	99.8	Detrital zircon
OPP_0036R_58	122	1.5	9.5511	1.9	4.6261	2.4	0.3206	1.5	0.62	1792.7	23.4	1754.0	20.3	1709.0	35.2	104.9	Detrital zircon
OPP_0036R_59	355	5.5	9.2678	1.3	4.6337	1.9	0.3116	1.4	0.74	1748.6	21.6	1755.4	16.0	1764.2	23.7	99.1	Detrital zircon
OPP_0036R_60	384	2.1	9.1241	1.6	4.8215	2.4	0.3192	1.8	0.74	1785.8	28.3	1788.7	20.6	1792.8	29.9	99.6	Detrital zircon
OPP_0036R_61	135	1.8	8.6505	1.9	5.4726	2.7	0.3435	1.9	0.71	1903.5	31.7	1896.3	23.2	1889.2	34.3	100.8	Detrital zircon
OPP_0036R_62	87	1.2	5.1073	1.8	14.2911	2.4	0.5296	1.6	0.68	2739.8	36.7	2769.2	23.0	2791.5	29.3	98.1	Detrital zircon
OPP_0036R_63	73	1.4	4.9285	1.8	15.3798	2.5	0.5500	1.8	0.72	2825.2	41.6	2839.1	24.2	2849.7	28.9	99.1	Detrital zircon
OPP_0036R_64	55	0.6	5.4377	1.5	13.3313	2.4	0.5260	1.9	0.79	2724.6	42.2	2703.4	22.7	2688.3	24.3	101.3	Detrital zircon
OPP_0036R_65	153	1.2	9.5420	1.5	4.4327	2.3	0.3069	1.7	0.74	1725.4	25.6	1718.5	18.9	1710.8	28.1	100.9	Detrital zircon
OPP_0036R_66	216	0.8	9.3371	1.9	4.5668	2.5	0.3094	1.7	0.68	1737.8	26.1	1743.2	21.1	1750.6	34.2	99.3	Detrital zircon
OPP_0036R_67	92	0.8	10.6952	2.6	3.2756	3.2	0.2542	1.9	0.60	1460.1	25.2	1475.3	25.0	1498.0	48.6	97.5	Detrital zircon
OPP_0036R_68	32	1.0	10.7066	2.7	3.2013	3.6	0.2487	2.4	0.67	1431.8	31.0	1457.5	27.9	1496.0	50.6	95.7	Detrital zircon
OPP_0036R_69	445	2.4	9.3633	1.6	4.6159	2.4	0.3136	1.8	0.75	1758.4	27.5	1752.1	20.0	1745.5	29.2	100.7	Detrital zircon
OPP_0036R_70	559	1.5	10.6045	1.8	3.4700	2.5	0.2670	1.8	0.70	1525.6	23.9	1520.4	19.9	1514.1	34.0	100.8	Detrital zircon
OPP_0036R_71	146	1.4	11.6822	2.2	2.6957	2.6	0.2285	1.4	0.55	1326.6	17.3	1327.3	19.6	1329.1	43.0	99.8	Detrital zircon
OPP_0036R_72	214	1.2	11.6550	2.0	2.7398	2.6	0.2317	1.7	0.66	1343.4	20.9	1339.3	19.6	1333.7	38.3	100.7	Detrital zircon
OPP_0036R_73	212	4.7	8.1235	1.9	6.0821	2.4	0.3585	1.5	0.63	1975.1	26.1	1987.7	21.1	2001.6	33.2	98.7	Detrital zircon
OPP_0036R_74	163	2.8	5.5127	1.5	12.6776	2.3	0.5071	1.7	0.75	2644.2	36.8	2656.0	21.2	2665.7	24.7	99.2	Detrital zircon
OPP_0036R_75	281	2.2	5.4318	1.6	12.5288	2.3	0.4938	1.7	0.74	2587.1	37.1	2644.9	22.1	2690.1	26.0	96.2	Detrital zircon
OPP_0036R_76	641	1.0	10.6157	1.5	3.3793	2.4	0.2603	1.8	0.78	1491.4	24.6	1499.6	18.6	1512.1	28.1	98.6	Detrital zircon
OPP_0036R_77	104	0.8	9.6246	2.1	4.0237	2.7	0.2810	1.6	0.61	1596.4	23.1	1639.0	21.8	1694.9	39.0	94.2	Detrital zircon
OPP_0036R_78	99	0.8	9.7087	2.0	4.0854	2.4	0.2878	1.3	0.54	1630.5	19.0	1651.4	19.8	1678.9	37.7	97.1	Detrital zircon
OPP_0036R_79	182	1.3	9.8039	1.7	4.1174	2.5	0.2929	1.8	0.74	1656.0	26.4	1657.8	20.1	1660.8	30.9	99.7	Detrital zircon
OPP_0036R_80	318	1.5	9.1912	1.7	4.3814	2.4	0.2922	1.7	0.69	1652.5	24.4	1708.8	20.0	1779.4	31.9	92.9	Detrital zircon
OPP_0036R_81	156	1.3	8.9445	1.8	4.8381	2.5	0.3140	1.8	0.70	1760.4	27.0	1791.6	21.1	1828.9	32.4	96.3	Detrital zircon
OPP_0036R_82	151	1.6	9.2937	1.6	4.5882	2.5	0.3094	2.0	0.78	1737.8	30.0	1747.1	21.1	1759.1	28.9	98.8	Detrital zircon
OPP_0036R_83	442	1.7	8.9526	1.3	4.6737	2.5	0.3036	2.1	0.84	1709.1	31.2	1762.5	20.7	1827.2	24.4	93.5	Detrital zircon
OPP_0036R_84	110	1.2	9.4877	2.4	4.2140	3.1	0.2901	2.0	0.64	1642.0	29.0	1676.7	25.5	1721.3	43.6	95.4	Detrital zircon
OPP_0036R_85	187	1.0	10.7643	1.6	3.2251	2.3	0.2519	1.7	0.72	1448.3	21.6	1463.2	18.0	1485.8	30.6	97.5	Detrital zircon
OPP_0036R_86	79	1.4	10.8460	2.0	3.1094	2.7	0.2447	1.8	0.69	1411.1	23.3	1435.0	20.6	1471.5	37.1	95.9	Detrital zircon
OPP_0036R_87	291	1.6	8.1699	1.3	5.8839	2.0	0.3488	1.5	0.76	1928.9	25.3	1958.9	17.4	1991.5	23.2	96.9	Detrital zircon

OPP-0036R (Quartzite)																	
Analysis	Isotope ratios								Apparent ages (Ma)							Observations	
	U	U/Th	206Pb <sup>a</sup> /	±	207Pb <sup>a</sup> /	±	206Pb <sup>a</sup> /	±	error	206Pb <sup>a</sup> /	±	207Pb <sup>a</sup> /	±	206Pb <sup>a</sup> /	±		
	(ppm)		207Pb <sup>a</sup>	(%)	235U <sup>a</sup>	(%)	238U	(%)	corr.	238U <sup>a</sup>	(Ma)	235U	(Ma)	207Pb <sup>a</sup>	(Ma)	(%)	
OPP_0036R_88	56	1.1	10.8578	2.4	3.2710	3.0	0.2577	1.8	0.61	1478.1	24.1	1474.2	23.4	1469.4	45.4	100.6	Detrital zircon
OPP_0036R_89	167	3.0	9.4518	1.5	4.2548	2.4	0.2918	1.9	0.78	1650.5	27.4	1684.7	19.9	1728.2	27.8	95.5	Detrital zircon
OPP_0036R_90	104	1.5	9.6061	1.9	4.1592	2.6	0.2899	1.8	0.68	1641.0	26.0	1666.0	21.5	1698.5	35.4	96.6	Detrital zircon
OPP_0036R_91	174	1.4	9.0827	1.6	4.7281	2.4	0.3116	1.8	0.73	1748.6	27.0	1772.2	20.2	1801.0	29.7	97.1	Detrital zircon
OPP_0036R_92	44	1.8	12.0627	3.5	2.4975	4.1	0.2186	2.1	0.52	1274.5	24.3	1271.3	29.6	1266.9	68.3	100.6	Detrital zircon
OPP_0036R_93	46	1.1	10.7296	2.5	3.1945	3.2	0.2487	2.0	0.63	1431.8	25.8	1455.8	24.6	1491.9	46.7	96.0	Detrital zircon
OPP_0036R_94	101	1.0	9.2937	2.1	4.5718	3.0	0.3083	2.1	0.70	1732.3	32.0	1744.2	25.0	1759.1	39.1	98.5	Detrital zircon
OPP_0036R_95	87	1.3	9.3897	2.2	4.3534	2.7	0.2966	1.6	0.59	1674.4	23.4	1703.5	22.1	1740.3	39.6	96.2	Detrital zircon
OPP_0036R_96	92	1.6	11.8203	2.2	2.5791	3.0	0.2212	2.0	0.67	1288.2	23.8	1294.7	22.2	1306.4	43.6	98.6	Detrital zircon
OPP_0036R_97	121	1.7	11.8483	2.4	2.5357	2.8	0.2180	1.5	0.53	1271.3	16.9	1282.4	20.3	1301.8	46.0	97.7	Detrital zircon
OPP_0036R_98	97	1.8	8.7260	2.0	5.2752	2.6	0.3340	1.7	0.64	1857.7	27.1	1864.9	22.3	1873.6	36.2	99.2	Detrital zircon
OPP_0036R_99	93	0.9	9.4518	2.2	4.1090	3.1	0.2818	2.2	0.72	1600.4	31.7	1656.1	25.5	1728.2	39.9	92.6	Detrital zircon
OPP_0036R_100	291	1.9	9.2593	1.6	4.5025	2.2	0.3025	1.5	0.69	1703.7	22.3	1731.4	18.0	1765.9	28.8	96.5	Detrital zircon